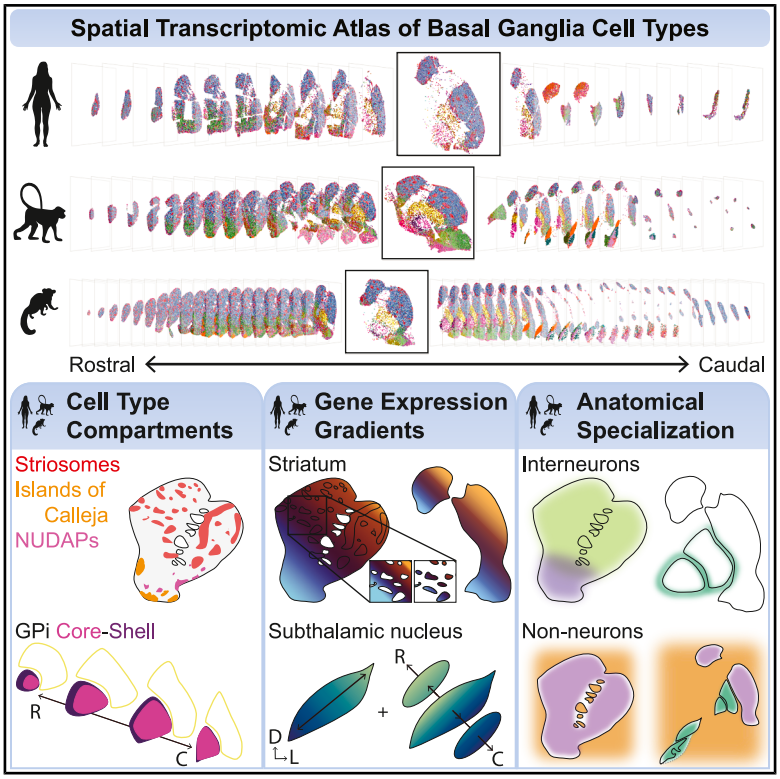
Cell

Article

Spatial transcriptomics reveals molecular organization of human and nonhuman primate basal ganglia

Graphical abstract



Highlights

- A cross-primate spatial transcriptomics atlas maps molecular organization of basal ganglia
- Anatomical specialization of interneurons and non-neurons is observed across primates
- Gene gradients span cell types in striatum and define organization of subthalamic nucleus
- Distinct cell types divide the internal globus pallidus into a conserved core and shell

Authors

Madeleine N. Hewitt, Meghan A. Turner, Nelson Johansen, ..., Jennie L. Close, Brian Long, Stephanie C. Seeman

Correspondence

jenniec@alleninstitute.org (J.L.C.), brianl@alleninstitute.org (B.L.), stephanies@alleninstitute.org (S.C.S.)

In brief

A cellular-resolution spatial transcriptomics atlas of the basal ganglia in human, rhesus macaque, and common marmoset highlights a conserved molecular organization and introduces an accessible resource for the research community. This atlas reveals complex gene expression gradients that coexist with discrete cell-type specializations.

Hewitt et al., 2026, Cell *189*, 7330–7349
November 12, 2026 © 2026 The Author(s). Published by Elsevier Inc.
https://doi.org/10.1016/j.cell.2026.10.023

CellPress

CellPress
OPEN ACCESS

Cell

Article

Spatial transcriptomics reveals molecular organization of human and nonhuman primate basal ganglia

Madeleine N. Hewitt,[1,14] Meghan A. Turner,[1,14] Nelson Johansen,[2] Delissa A. McMillen,[1] Shu Dan,[3] Michael DeBerardine,[3] Augustin Ruiz,[1] Mike Huang,[1] Jacob Quon,[1] Yuanyuan Fu,[2] Inkar Kapen,[2] Stuard Barta,[1] Naomi Martin,[1] Nasmil Valera Cuevas,[1] Paul Olsen,[1] Josh Nagra,[1] Jazmin Campos,[1] Marshall M. VanNess,[1] Shea Ransford,[1] Zoe Juneau,[1] Sam Hastings,[1] Lindsey Ching,[1] Michael Kunst,[1] Soumyadeep Basu,[4,5] Thomas Höllt,[5] Chang Li,[4] Boudewijn Lelieveldt,[4,5] Faraz Yazdani,[6] Qiangge Zhang,[7,8] Kirsten Levandowski,[7,8] Guoping Feng,[7,8] Burke Q. Rosen,[9] Matthew F. Glasser,[10] Takuya Hayashi,[11,12] Aaron D. Garcia,[2] Omar Kana,[1] Zoe M. Maltzer,[1] Luke Campagnola,[1] Tim Jarsky,[1] Lauren Kruse,[1] Winrich Freiwald,[6] C. Dirk Keene,[13] David C. Van Essen,[10] Jeanelle Ariza,[1] Jack Waters,[1] Fenna M. Krienen,[3] Trygve E. Bakken,[2] Rebecca D. Hodge,[2] Lydia Ng,[1] Hongkui Zeng,[1] Ed S. Lein,[2] Jennie L. Close,[1,*] Brian Long,[1,*] and Stephanie C. Seeman[1,15,*]

[1]Allen Institute, Brain Science, Seattle, WA, USA
[2]Allen Institute, Brain Health, Seattle, WA, USA
[3]Princeton Neuroscience Institute, Princeton University, Princeton, NJ, USA
[4]Leiden University Medical Center, Leiden, the Netherlands
[5]Delft University of Technology, Delft, the Netherlands
[6]Laboratory of Neural Systems, the Rockefeller University, New York, NY, USA
[7]McGovern Institute for Brain Research, Department of Brain and Cognitive Sciences Massachusetts Institute of Technology, Cambridge, MA, USA
[8]Stanley Center for Psychiatric Research, Broad Institute of Massachusetts Institute of Technology and Harvard, Cambridge, MA, USA
[9]Department of Neuroscience, Washington University in St. Louis, St. Louis, MO, USA
[10]Washington University School of Medicine, St. Louis, MO, USA
[11]Laboratory for Brain Connectomics Imaging, RIKEN Center for Biosystems Dynamics Research, Kobe, Japan
[12]Department of Brain Connectomics, Kyoto University Graduate School of Medicine, Kyoto, Japan
[13]University of Washington BioRepository and Integrated Neuropathology (BRaIN) lab, Harborview Medical Center, Seattle, WA, USA
[14]These authors contributed equally
[15]Lead contact
*Correspondence: jenniec@alleninstitute.org (J.L.C.), brianl@alleninstitute.org (B.L.), stephanies@alleninstitute.org (S.C.S.)
https://doi.org/10.1016/j.cell.2026.10.023

SUMMARY

The basal ganglia (BG) are interconnected subcortical nuclei with a complex topographical organization that orchestrate goal-directed behaviors and are implicated in neurodegenerative movement disorders. We generated a cellular-resolution spatial transcriptomics atlas of the BG in human, rhesus macaque, and common marmoset, sampling over one million cells in each species. By integrating spatial data with a cross-species consensus single-nucleus RNA sequencing (snRNA-seq) cell-type taxonomy, this atlas reveals principles of molecular organization within and across structures. Extensive spatial sampling across the rostral-caudal axis illuminates complex, yet highly stereotyped, multi-axis gene expression gradients superimposed onto discrete compartments of the striatum. Additionally, we identify core-shell organization of the internal globus pallidus. This unified, cross-species spatial transcriptomics atlas will be a foundational resource for characterizing the molecular and functional organization of the BG and their roles in health and disease.

INTRODUCTION

The basal ganglia (BG) are a group of deep subcortical nuclei critical for motor control, decision-making, and reward processing that have yet to be comprehensively profiled and compared across primates. These nuclei (including the striatum [STR], globus pallidus [GP], subthalamic nucleus [STH], and substantia nigra [SN])[1] are also central to the pathophysiology of several major neuropsychiatric and neurodegenerative diseases, including Parkinson's disease, Huntington's disease, and addiction, making a detailed understanding of their cellular organization a priority for both basic and translational neuroscience.[2,3]

This is an open access article under the CC BY license (http://creativecommons.org/licenses/by/4.0/).

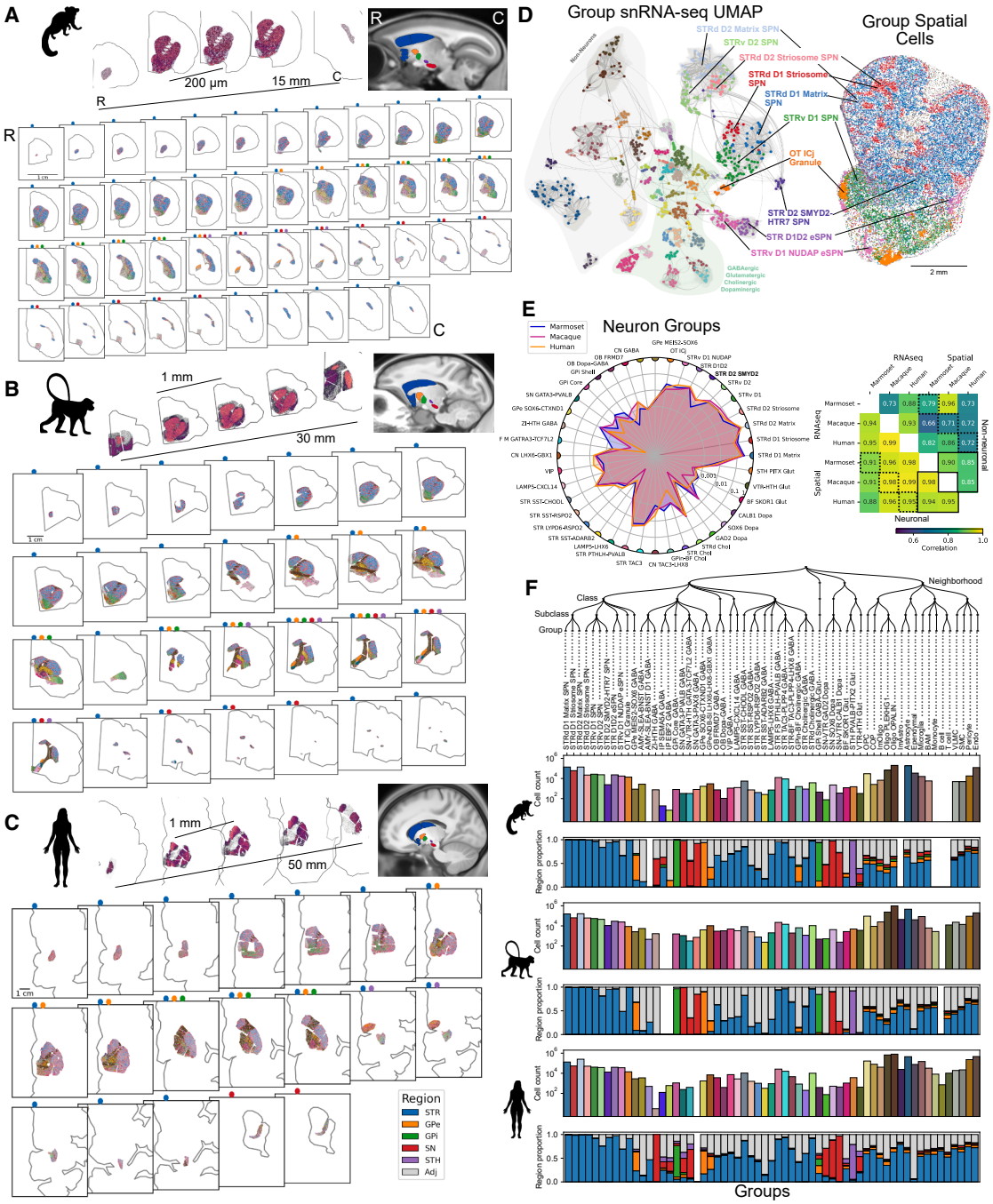


Figure 1. Cross-species basal ganglia spatial transcriptomics atlas

(A–C) Spatial transcriptomic sampling of the basal ganglia (BG) in three primates: common marmoset (A), rhesus macaque (B), and human (C). The top row depicts *DRD1* expression in sections spanning the rostral (R) to caudal (C) ends of the sampling range and 3 middle sections depicting the sampling interval. To the left is a template sagittal view with BG common coordinates framework (CCF) regions overlaid for reference. Below, all sections collected are ordered from R to C with an outline of the full hemisphere. Spatial transcriptomic cells are colored by Group following the colors in (D) and the color bars in (F). Colored dots above each section indicate the BG regions sampled. Scale bar is 1 cm.

(D) Left, uniform manifold approximation and projection (UMAP) of a cross-species consensus taxonomy where each dot is a cluster, colored by Group membership. Right, spatial section of the marmoset striatum showing corresponding taxonomy Groups in the spatial data. Each point is a cell colored by its Group. Scale bar is 2 mm.

(E) Comparison of Group proportions in spatial transcriptomics across species. The radar plot (left) includes all species, and each point is the number of cells in that Group as a fraction of all neuronal Groups plotted on a log scale. Heatmap (right) shows Pearson correlation of these populations across species and

(legend continued on next page)

Classical descriptions of BG cell-type organization have largely relied on anatomical studies using histochemical staining and tract tracing to identify neuronal cell types and map their connectivity.[4–9] Although these approaches have generated foundational anatomical knowledge, they are inherently limited in resolution, as the number of stains that can be simultaneously measured is small. Further, the molecular markers for functionally homologous cell types are not always conserved, making cross-species comparisons difficult.[10,11]

Single-cell transcriptomic technologies have provided unprecedented molecular detail of the cellular composition of the mammalian brain[12–15] and have begun to link cell types across species.[11,16–18] Recent studies have sampled portions of the BG in individual primate species,[12,19,20] building a foundation for cell-type composition in these regions, albeit with broad, disparate cell-type nomenclature and sparse linkages across species. Furthermore, tissue dissociation limits the ability of single-cell transcriptomic approaches to place these cell types in a precise spatial context, which is critical in subcortical regions with complex anatomical organization such as the BG.

Modern spatial transcriptomic techniques can provide the link between these molecular identities and the well-characterized neuroanatomical and topographic organization of the core BG nuclei. To this end, we have generated a comprehensive, cellular-resolution spatial transcriptomics atlas of BG cell types across marmoset, macaque, and human. By integrating our spatial transcriptomics data with a consensus cell-type taxonomy,[21] morphological and electrophysiological data,[22] and a harmonized ontological schema,[23] we provide a unified, multimodal characterization of primate BG cell types. In this study, we characterize cell-type localization, explore gene expression gradients, and perform interspecies comparisons of anatomical cell-type organization. Overall, we find a consistent molecular organization of BG nuclei that spans orthogonal yet overlapping axes. By integrating our data into online visualization platforms and analysis tools, we provide an accessible resource that can serve as a common framework for future BG research.

RESULTS

A cross-primate spatial atlas of the BG

We present a cross-species spatial transcriptomics atlas of the BG (Figures 1A–1C), a key component of a multimodal resource atlas characterizing this subcortical region. We designed a robust and standardized workflow to ensure the reproducibility and harmonization of this spatial dataset across species (Figure S1). Central to our ability to compare across species is the BG Cross-Species Consensus Taxonomy,[21] which is hierarchically organized at five levels of increasing granularity: cross-species Neighborhood, Class, Subclass, Group, and species-specific clusters (Table S1). This taxonomy is not only cross-species but also inherently cross-modal: the spatial transcriptomics atlas described here, along with the electrophysiological and morphological characterization described in Liu et al.,[22] provided anatomically and functionally anchored definitions and nomenclature for the initial transcriptomically clustered cell types (Figure 1D). Cross-species integration and annotation in transcriptomic space provides a unified taxonomy of BG cell-type identity with common nomenclature across marmoset, macaque, and human.[21]

We linked cell-type identities to cells in our spatial transcriptomics data by assigning each spatial cell to the most similar species-specific cluster in the taxonomy. Each spatial cell then inherits unified Group, Subclass, Class, and Neighborhood labels while accommodating species-specific details of gene expression. To achieve robust annotation of cell types in our spatial dataset, we designed species-specific gene panels, with 300 genes each. The full gene panel was used to map to the taxonomy using MapMyCells (RRID: SCR_024672), and shared genes (STAR Methods; Table S2) enabled a cross-species comparison of spatial gene expression patterns. Confusion matrices for single-nucleus RNA sequencing (snRNA-seq) cells self-mapped back to the taxonomy using just the genes in each species' panel show a strong diagonal (Figures S2A–S2C), providing confidence for cell-type assignment in the spatial data. Further, comparing F1 scores between self-mapping using the spatial gene panels and the full transcriptome shows that we are near the limit of cell-type identification set by the snRNA-seq taxonomy itself (Figures S2D–S2F).

The resulting BG spatial transcriptomics atlas includes more than eight million cells across nearly 100 coronal sections. We sampled the STR, GP external (GPe) and internal (GPi) segments, SN, and STH through the full rostral-to-caudal (R-C) extent in one hemisphere of each species (Figures 1A–1C). In marmoset, we collected 46 sections with an inter-section interval of 200–600 μm (Figure 1A; STAR Methods); in the larger macaque and human brains, a 1-mm sectioning interval resulted in 32 sections and 19 sections, respectively (Figures 1B and 1C). Following spatial transcriptomics imaging, post-processing workflows (Figures S1C–S1H) harmonized our data across species for downstream analysis (STAR Methods; Figures S3 and S4). We analyzed 1.3 million cells in marmoset, 3.1 million cells in macaque, and 4.0 million cells in human. We focused our analysis on the Group level of the taxonomy, the finest level of cell-type resolution that is transcriptomically conserved across species. Neuronal Group proportions are highly correlated across species in spatial transcriptomics and snRNA-seq as well as between modalities (Figure 1E, right), validating the transcriptomic classification. Though Group cell abundances are generally consistent across species, we do find species differences in individual Groups. The newly described STR D2 SMYD2-HTR7 SPN Group (Figure 1E, left, bolded) is a rare type that transcriptomically resembles both matrix and striosome spiny projection neurons (SPNs) and is uniformly distributed across both the matrix and striosome compartments of the dorsal striatum (STRd).[21] This Group is three times as

modalities for neuronal (lower left half) and non-neuronal (upper right half) cells. Solid lines denote cross-species, within-spatial correlation; dotted lines denote within-species, cross-modality correlation.

(F) BG transcriptomic hierarchy terminating at the species-conserved Group level (top). Each pair of plots below shows the cell count and region proportions for each Group in each species. Full Group names are used in (F) and short Group names in (E) for visibility (see Table S1).

abundant in macaque and human compared with marmoset in both modalities (Figure 1E, left; Figure S5A) and represents approximately 1.5% of all neuronal cells in macaque and human versus 0.5% in marmoset (Table S3). Our spatial transcriptomics atlas enables analysis beyond cell-type proportions: we can now characterize the precise anatomical distributions of cell types in each species (Figure 1F; Figure S5B; Tables S4–S6, and S7).

Regional specialization of cholinergic interneurons in the BG

Inhibitory interneuron Groups of the medial (MGE) and caudal (CGE) ganglionic eminences lineages show varied regional distributions (Figure S6), including dispersed distributions like that of STR FS PTHLH-PVALB GABA and more spatially constrained cholinergic Groups. Previous work has characterized striatal cholinergic neurons functionally and morphologically and has suggested that they exist along a dorsal-ventral gradient,[24] though a molecular distinction between dorsal and ventral subpopulations has not been established.[25,26] Our atlas identifies two transcriptomically distinct cholinergic Groups in STR that are anatomically biased toward the STRd (STRd Cholinergic GABA) or the ventral striatum (STRv) (STR Cholinergic GABA) (Figure 2A). A third cholinergic Group, GPin-BF Cholinergic GABA, is specifically found in the lamina surrounding the GPe and GPi as well as in the basal forebrain (BF) (Figure 2B). This pattern is most evident in the marmoset, where we have finer rostral-caudal resolution through this structure and can observe a narrow band of cholinergic cells in the lamina between the GPe and GPi. We now provide a more complete molecular identity for these cells, previously described as the Ch4 cell type in cytoarchitectural studies.[27–29]

Regional specialization of glial cell types in the BG

Non-neuronal cells comprise their own Neighborhood of the consensus taxonomy, and while many non-neuronal cell types are more broadly distributed across BG structures than their neuronal counterparts (Figure 1F; Figure S7), certain glial Groups show an anatomical bias in their distributions. Mature oligodendrocytes are split into two Groups with distinct molecular signatures, Oligo PLEKHG1 and Oligo OPALIN,[30,31] that also have different spatial distributions in the BG. Oligo OPALIN is highly enriched in striatal gray matter, whereas Oligo PLEKHG1 is more enriched in white matter, especially in the internal capsule (Figure 2C). The GPe and GPi, structures with higher white matter content, show a spatial gradient of enrichment between these two Groups.

Two companion studies report that Clusters within the Astrocyte Group also show anatomical segregation between white matter and gray matter in human[32] and marmoset.[33] We extend that finding here to macaque and show that this is a consistent spatial organization of BG astrocytes across primate species. Three macaque Clusters make up the majority of the Astrocyte Group and are spatially segregated to the gray matter of the STR (Macaque-257), the gray matter of extrastriatal nuclei (Macaque-231), or white matter (Macaque-232) (Figure 2D).

Spatial organization of SPNs in the STR

The primary neuronal cell type of the STR is the SPN, a lateral ganglionic eminence (LGE)-derived, inhibitory projection neuron. As expected, we find SPNs predominantly in the STR, though they are also found in neighboring regions, such as the amygdalostriatal transition area (AStr), which are often overlooked in single-region studies. Subpopulations of striatal SPNs are biased toward the STRd, biased toward the STRv, or dispersed throughout the STR; taxonomy Group nomenclature reflects these anatomical distributions (Figure S5B). SPNs that predominantly localize to the nucleus accumbens (NAC) and olfactory tubercle (OT) are pooled into encompassing STRv Groups (STRv D1 SPN and STRv D2 SPN). STRd SPNs are further organized along two classical, orthogonal axes: D1 versus D2 dopamine receptor expression and matrix versus striosome localization (Groups STRd D1 Matrix SPN, STRd D1 Striosome SPN, STRd D2 Matrix SPN, and STRd D2 Striosome SPN). These consensus STRd Groups are found across the caudate and putamen.

Compartmental organization of striatal neurons

In addition to the dorsal-ventral and D1-D2 organizing axes, the primate STR is organized into four compartments: striosomes and the surrounding matrix, Islands of Calleja (ICjs), and neurochemically unique domains found in the nucleus accumbens and putamen (NUDAPs). Although these compartments were originally defined by neuro- or histochemical staining,[34,35] modern molecular techniques have since described distinct transcriptomic cell types associated with each compartment in mouse[36] and macaque.[19] Our cross-species atlas identifies conserved transcriptomic Groups that localize to each compartment (Figure 3A): STRd D1 Striosome SPN and STRd D2 Striosome SPN in striosomes; STRd D1 Matrix SPN and STRd D2 Matrix SPN in matrix; STRv D1 NUDAP eSPN in NUDAPs; and OT ICj Granule in ICjs. We used the cell density of these Group labels to define the boundaries of the striosome, NUDAP, and ICj compartments in each section (Figure 3B; STAR Methods).

We quantified the enrichment of all striatal neuronal Groups in the three compartments (Figures S8A–S8C; STAR Methods). In striosomes, we find, as expected, enrichment of STRd D1 and D2 Striosome SPNs, and depletion of STRd D1 and D2 Matrix SPNs. Notably, one interneuron Group, STR TAC3-PLPP4 GABA, is depleted (Figure 3C) and visibly absent from striosomes (Figure 3D) in all three species. In NUDAP compartments, along with the expected STRv D1 NUDAP eSPNs, another eccentric SPN Group, STR D1D2 eSPN, is enriched in NUDAP compartments in marmoset and macaque (Figures S8B, S8D, and S8E).

We also find compartment-associated cells outside of their compartment boundaries. For instance, OT ICj Granule cells are found both within the ICjs and as individual cells scattered throughout the OT and BF (Figure 3E). In human, the proportion of these scattered, ''exo-compartment'' OT ICj Granule cells is significantly higher (39%) than in marmoset (17%) or macaque (8%) (Figure S8F). Cytoarchitectonic studies of human OT previously described exo-island granule cells,[37] and our atlas now establishes that these are the same molecular cell type that is localized to the ICjs.

Sparse striosome-like SPNs observed in the matrix

In all three species' data, we observed a subset of STRd D1 Striosome SPN and STRd D2 Striosome SPN cells outside of striosome compartment masks within individual two-dimensional

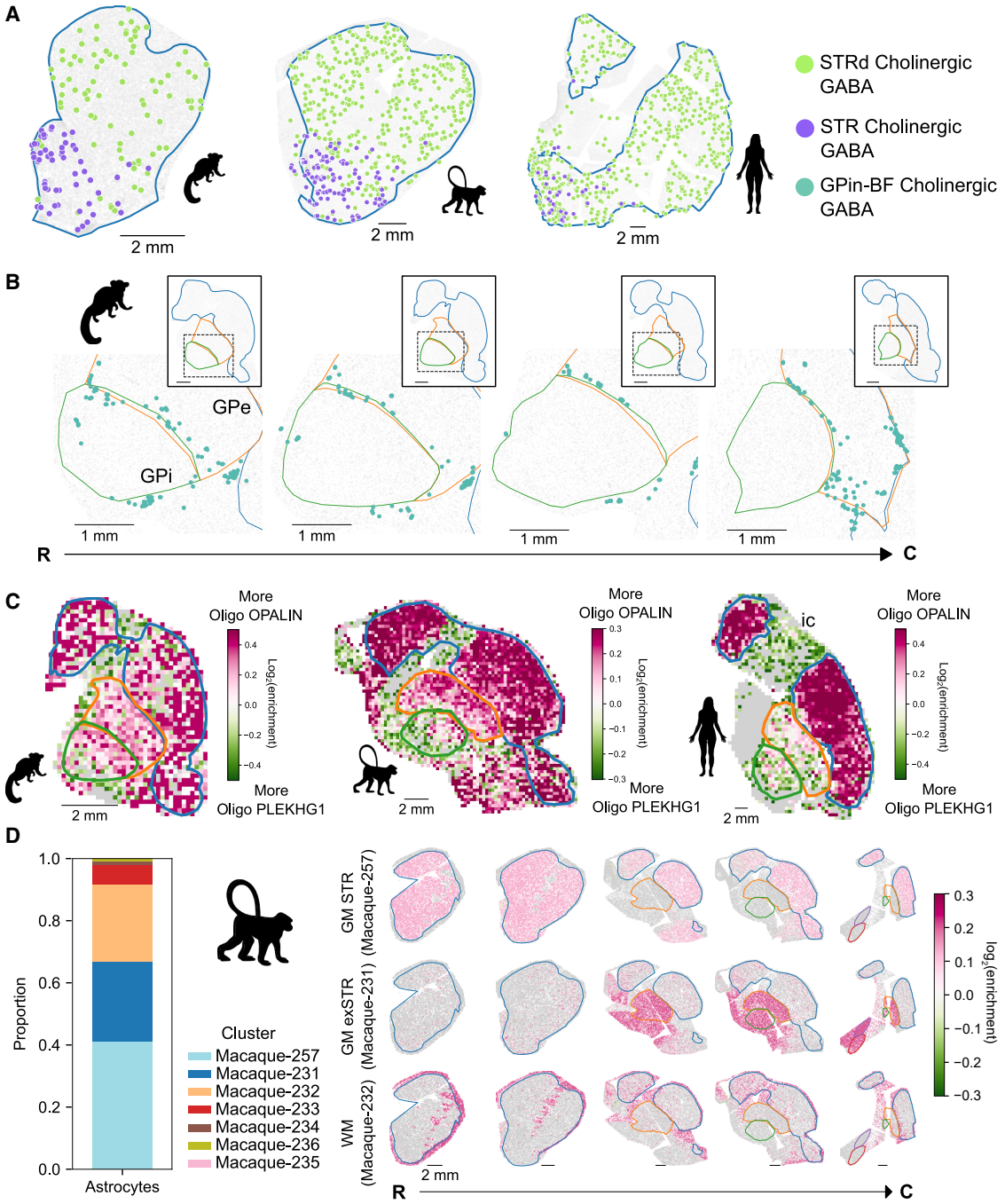


Figure 2. Spatial specialization of interneurons and non-neurons in the BG

(A) Two cholinergic Groups in the striatum (blue outline) are biased toward the dorsal striatum, STRd Cholinergic GABA (green), and the ventral striatum, STR Cholinergic GABA (purple) in all three species. Scale bars represent 2 mm.

(B) A third cholinergic Group, GPin-BF (teal), is specifically found in the lamina between the GPe (orange outline) and GPi (green outline), shown here through multiple sections in marmoset. Zoom-outs in the upper right show the full section with a dotted box outlining the zoom-ins. Scale bars represent 1 mm.

(C) Two oligodendrocyte Groups show enrichment toward gray matter or white matter. Oligo OPALIN (pinker areas) is enriched in the gray matter of the striatum (blue outline) and is less so in the GP (orange and green outlines), whereas Oligo PLEKHG1 (greener areas) is more enriched in the white matter of the internal capsule. Scale bars represent 2 mm.

(D) Astrocyte clusters are also enriched in gray matter versus white matter. In macaque, 3 Astrocyte clusters make up >90% of the Group (left; Macaque-257, -231, and -232). Macaque-257 is enriched in striatal gray matter (blue outline, right top), Macaque-231 is enriched in extrastriatal gray matter (right, middle), and Macaque-232 is enriched in white matter (right, bottom). In all panels, colored outlines denote regional annotations: STR (blue), GPe (orange), GPi (green), STH (purple), and SN (red). Scale bars represent 2 mm.

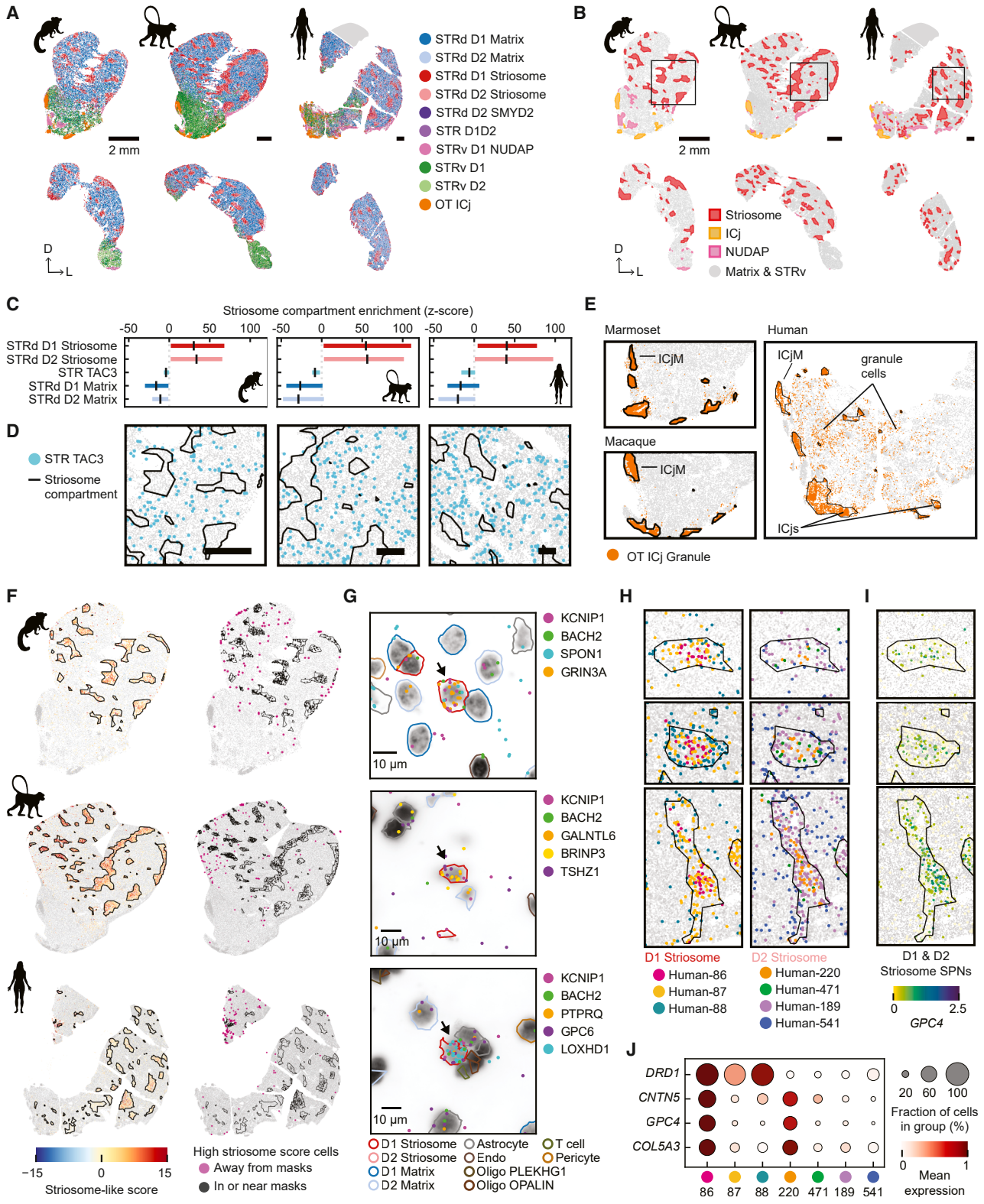


Figure 3. Discrete cell types and compartments of the striatum

(A) The ten predominant neuronal Groups in the striatum, shown at one rostral (top) and one caudal (bottom) slab-plane in each species (from left to right: marmoset, macaque, human). Scale bars represent 2 mm.

(legend continued on next page)

slab-planes (Figures 3F and 3G; Figure S8G). To account for cells that could have just been excluded by the striosome mask boundary definitions, we filtered out cells that were close to a striosome mask (<100 μm in marmoset, 200 μm in macaque, and 400 μm in human). Furthermore, Striosome and Matrix SPNs exist along a transcriptomic spectrum, with potential for confusion where their transcriptomic profiles overlap (Figures S9A–S9G). To account for cells that fall within this overlap, we then filtered out any cells below a minimum striosome-like gene expression score (<mean + 1 SD of the log-odds distribution of all striosome-like cells; absolute score values of <5.5 in marmoset, 8.9 in macaque, and 5.6 in human). These criteria allowed us to confidently identify a small proportion of cells (1.4% of all Striosome SPNs in our marmoset data, 1.1% in macaque, and 1.0% in human) that are both far away from any striosome mask in the same 2D plane and have strong striosome-like gene expression (Figure 3F; Figures S9E–S9H; STAR Methods). These exemplar Striosome SPNs in the matrix express visibly high levels of striosome marker gene transcripts, including established markers such as *KCNIP1*,[38] in stark contrast to their Matrix SPN neighbors (Figure 3G; Figures S10A and S10B).

Internal organization of human striosomes

Previous histochemical staining has shown that human striosomes are internally organized into an inner "core" zone and an outer "annulus" zone.[39] We find a transcriptomic analog of this organization: at the finest level of our taxonomy, species-specific Clusters form overlapping radial layers with some biased to the core and others biased to the annulus (Figure 3H; Figures S10C–S10F). The radial organization is most strongly observed in human (Figures S10C and S10E–S10H), where multiple genes are differentially expressed in the two innermost core clusters (Figures 3I and 3J; Figure S10D). This finding highlights a tight correspondence between observations from histological staining and cellular molecular signatures captured in our atlas.

Gene expression gradients in the STRd transcend compartment boundaries

Our spatial transcriptomics atlas presents a unique opportunity to explore the molecular aspects of SPN diversity by both identifying discrete molecular organization (Figure 3) and placing continuously varying gene expression into anatomical context. The circuit functions of the rostral STR are distributed along a dorsal-ventral axis in striatal substructures (caudate, putamen, and NAC) with corticostriatal projections exhibiting regionally varying but diffuse innervation of the STR.[5,40] In parallel, previous descriptions of gene expression in rodents and primates have observed analogous dorsal-ventral gradients.[19,36] In mouse, these have been described as either one[36] or two opposing[41] gene programs (Figure S11A).

To address spatial variation of gene expression in the STR, we applied non-spatial principal component analysis (PCA) to all cells in the canonical SPN Groups and identified the principal component (PC) with the largest spatial gradient in each species, which we term "PCg" (gradient PC) (Figure S12; STAR Methods). Although some other PCs also show spatial variation (Figure S12A), PCg captures graded gene expression variation across multiple anatomical axes. In coronal planes of the STRd, PCg is directed along a ventral-medial to dorsal-lateral axis (VM-DL) roughly parallel to the internal capsule and extends across the rostral-caudal axis (Figure 4A). When subset to the individual STRd D1/D2 and Striosome-Matrix Groups, PCg shows a consistent VM-DL direction across sections (Figure 4B). PCg thus reflects a gene expression pattern that spans direct- and indirect-pathway neurons in both striosome and matrix compartments. The in-plane direction of PCg and its average value in each Group is also highly correlated across the R-C extent of our sampling (Figure 4C). We see coordinated rotation of the in-plane PCg direction in the rostral-most sections of marmoset, but we do not observe similar variation in macaque or human, which may be the result of finer sampling in marmoset.

We investigated the underlying gene expression, including four gradient genes common to the gene panels in all species (Figure 4D; Figure S11B). Although these genes share the overall gradient, they did not exhibit identical spatial profiles, as seen in the half-maximum positions of each gene (white dots in Figure 4E). For example, in macaque, *TESPA1* and *CNR1* both peak in the dorsal-lateral putamen, but *CNR1* decreases gradually toward the STRv, whereas *TESPA1* is concentrated in the dorsal-lateral putamen. The finding that genes show varying

(B) Polygon masks of three compartments: striosomes (red), ICjs (orange), and NUDAPs (pink) in the same slab-planes as in (A). Scale bars represent 2 mm.
(C) *Z*-scored enrichment of Groups in striosome compartments. Positive values indicate enrichment (STRd D1 and D2 Striosome SPNs) and negative values indicate depletion (STR TAC3-PLPP4 GABA interneurons and STRd D1 and D2 Matrix SPNs). Calculated per slab-plane with the colored bar showing the span from minimum to maximum slab-plane score and the black bar indicating the mean score.
(D) Spatial distribution of STR TAC3-PLPP4 GABA interneurons relative to striosome compartment boundaries shows that this cell type is depleted in striosomes in all three species (from left to right: marmoset, macaque, and human). Zoomed-in region indicated by the black box in (B).
(E) OT ICj Granule cells are present outside of ICj compartments in marmoset and macaque (left) but are more prevalent in human (right).
(F) Striosome score (left) and distance from the striosome boundary were used to identify a candidate subpopulation of the STRd D1 and D2 Striosome SPN Groups that are found outside striosome masks (right; magenta cells). The striosome score is a logistic regression classification score where more positive values indicate a strong Striosome SPN cell-type identity and more negative scores a strong Matrix SPN cell-type identity.
(G) Striosome marker gene expression in a representative striosome-like cell found outside the striosome masks (indicated with a black arrow) in each species (top to bottom: marmoset, macaque, and human). The black-and-white image is a DAPI nuclear stain. Cell segmentation outlines are colored by Group label. Scale bars represent 10 μm.
(H) Clusters of STRd D1 Striosome SPN (left) and STRd D2 Striosome SPN (right) Groups in three representative human striosomes. These clusters are organized in an overlapping radial pattern inside the striosomes.
(I) *GPC4* gene expression (batch normalized and natural logarithmized) in the same striosomes as in (H).
(J) Dot plot showing mean expression and fraction expressing for four genes (*DRD1*, *CNTN5*, *GPC4*, and *COL5A3*) in the seven striosome clusters shown in (H). *DRD1* expression is included to indicate which clusters belong to the STR D1 Striosome SPN Group.

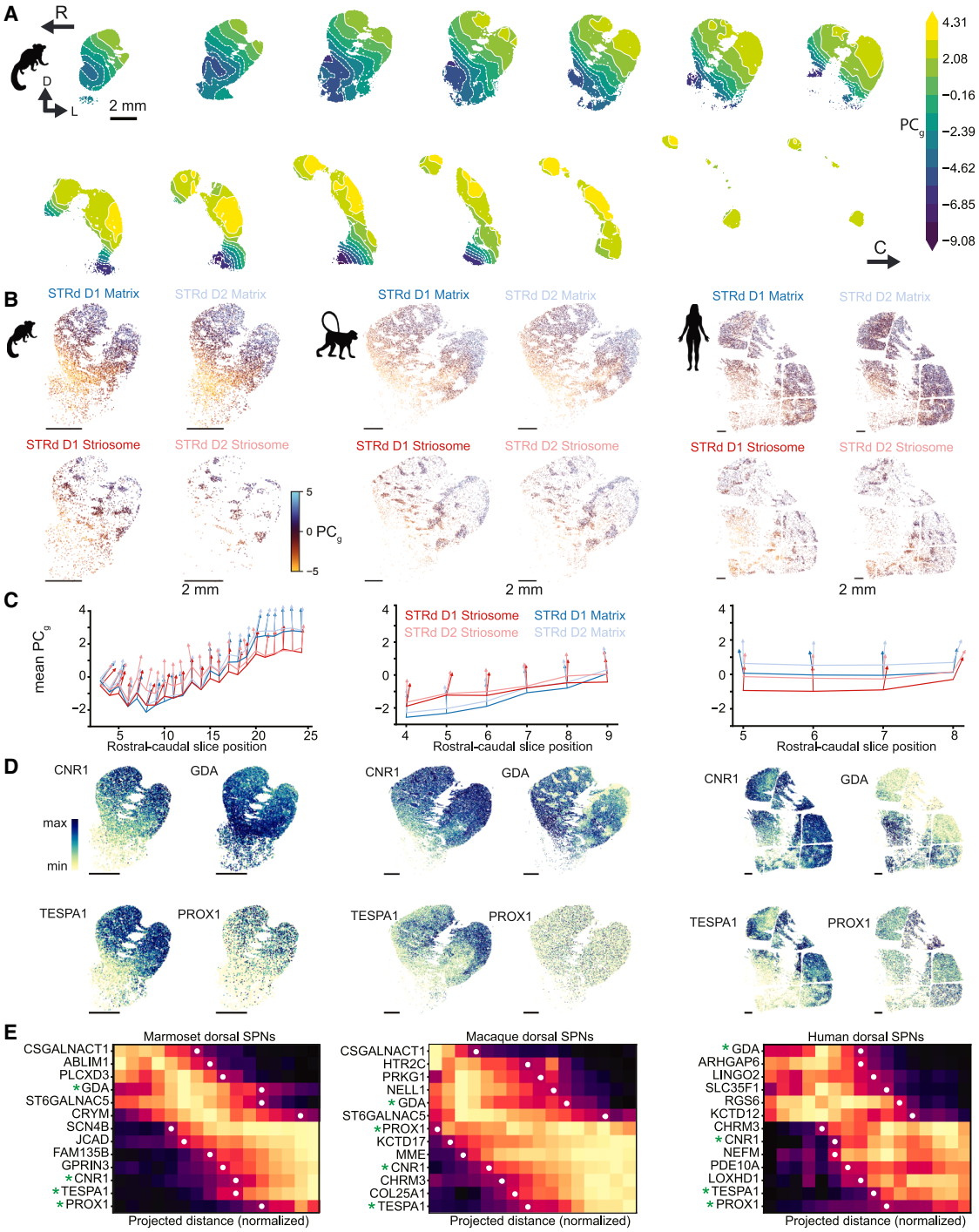


Figure 4. Continuous gene expression variation in the striatum

(A) Contour plot showing the variation of the gradient principal component (PCg) in marmoset SPNs across the rostral-caudal extent. PCg variation is broadly aligned with the internal capsule but also has minima in the medial accumbens shell and the ventral caudate tail. Scale bar represents 2 mm.

(B) Dorsal SPN Groups show a common spatial gradient structure. Dorsal SPN Group cells colored by PCg value share an overall gradient direction, independent of striosome-matrix or D1/D2 Group status. Scale bars represent 2 mm.

(legend continued on next page)

spatial profiles across the STR, rather than changing in lockstep, indicates that PCg may contain multiple gene programs. A companion study[42] shows a similar VM-DL spatial gradient in the human STR using a whole-transcriptome assay in a different donor, corroborating the central role of a spatial gradient in the organization of gene expression in the STR.

Some genes represented in PCg have relatively well-understood functions in neurons, such as the cannabinoid receptor *CNR1*, the serotonin receptor *HTR2C*, and the PSD-95-associated guanine deaminase *GDA*.[43] The gradient of *CNR1* has been associated with other genes in mouse[36] and in our companion paper across primate species.[21] PCg also includes genes whose roles in neuronal circuits are far less explored, such as *ST6GALNAC5*, which encodes an enzyme involved in ganglioside modification, and *CSGALNACT1*, which participates in chondroitin sulfate synthesis and was associated with ventral clusters of SPNs in mouse.[41] One gene that follows PCg in all three species, *TESPA1*, is involved in controlling intracellular calcium in response to T cell receptor activation,[44] but its limited footprint in the literature does not include a neuronal function. The robust spatial variation of these genes suggests that they are important for BG circuit organization and may reflect underappreciated or unknown functions.

Molecularly distinct regions in the STRv anchor the multi-axis gradient

The rostral STRv, which includes the NAC and OT (Figures 5A–5C; Figure S13), is associated with limbic connectivity and function.[1] Regions of the caudal STR, including the caudate tail (CaT) and caudoventral putamen (PuCv) (Figures 5D–5F), have limbic connectivity and similar molecular properties to the rostral STRv.[4,45] These regions have therefore often been considered part of the ventral (limbic) STR, including in a companion paper.[23]

Our data support a shared ventral cell-type identity across the rostral and caudal STRv. We find STRv D1 and D2 SPNs not only in the NAC and OT (Figures 5A–5C, inset) but also across the longitudinal axis of the caudate—particularly CaT—and in the caudal putamen (Figures 5D–5F). PCg, a measure of dorsal-ventral SPN identity, corroborates this finding: upon aggregating per-cell PCg scores and viewing them as a topographic map, the high and low values of the gradient occur in similar locations across aligned coronal sections, with the low values coinciding with the locations of STRv D1 and D2 SPNs (Figures 5A–5F; Figure S13). This suggests that ventral SPN identity is not restricted to a contiguous rostral subregion (i.e., the NAC and OT) but instead occurs across the rostral-caudal extent of the STR, reflecting a common ventral molecular program.

Specific subregions in the STRv anchor the gradient. In the rostral STRv, the lowest PCg values occur in the mediodorsal NAC shell (NACsmd) (Figures 5A–5C). The NACsmd is a triangular region of the STRv below the ventricle that has previously been shown to have unique connectivity and molecular properties.[25,46–49] Each species has at least one STRv D1 SPN cluster that localizes specifically to the NACsmd (Marmoset-95: Macaque-9, and -10; Human-215 and -216) (Figures 5G–5I; Figures S14A–S14C). Analysis of the corresponding Clusters in snRNA-seq and spatial data reveals several differentially expressed genes compared with other STRv D1 SPNs (Figures S14A–S14C). Macaque D1 SPNs in NACsmd exhibit higher *TAC3* expression (Figures S14B and S14E), consistent with previous observations.[19] Across species, NACsmd-specific clusters also have lower expression of the pan-SPN marker *PPP1R1B* than other STRv D1 SPNs (Figure S14). These results suggest that D1 SPNs in NACsmd exhibit molecular specialization.

A similar trend is observed in the caudal STR: low PCg values are found in SPNs between the CaT and the central nucleus of the amygdala (CEN), suggesting a corresponding "anchor" (Figures 5D–5F). We identify this region as the AStr, which is characterized by unique STRv D2 SPN clusters (Marmoset-996, -1006, -1007, -1008, and -1012; Macaque-406 and -407; Human-332, -334, -335, and -508) (Figures 5J–5L, left; Figures 15A–15C). Similar to NACsmd clusters, AStr clusters exhibit distinct gene expression profiles compared with other STRv D2 SPNs in both snRNA-seq and spatial data, including lower *PPP1R1B* expression (Figure S15). Additionally, the AStr exhibits a high proportion of D2 SPNs (compared with D1) (Figures 5J–5L, right). The AStr therefore parallels the NACsmd in terms of its position within the striatal gradient and distinct gene expression (particularly *PPP1R1B*; Figure S15). In contrast to the NACsmd, however, the AStr is enriched in D2 SPNs, many of which belong to AStr-specific clusters. This parallels findings in mouse,[50] where the AStr was found to be enriched in D2 SPNs that are genetically distinct from those in the CEN and tail of the STR; AStr neurons were also shown to be physiologically and functionally distinct from neurons in these adjacent regions. Regions that are anatomically and molecularly positioned as transition zones can nonetheless have distinct molecular properties and functions, which can only be fully appreciated when neighboring regions are considered together in their spatial context.

Molecular organization of the STH mirrors functional gradients

The STH contains overlapping functional domains along its longitudinal VM-DL axis.[51,52] Recent studies in mouse and macaque have shown that the molecular organization of the STH parallels these topographical gradients of connectivity.[53–56] We find that marmoset and human also share this key principle of spatial organization in STH cell types and gene expression.

The cells of the STH belong to a single, glutamatergic Group in our consensus taxonomy, STH PVALB-PITX2 Glut (Figure 6A),

(C) Gradient direction is highly correlated among dorsal SPN Groups across the rostral-caudal extent. Mean PCg value (*y* axis) and direction (arrows) are shown for each dorsal SPN Group across rostral-caudal sections (*x* axis). The PCg values and gradient angles are correlated across dorsal SPN Groups (mean Pearson's r: PCg value: marmoset 0.97, macaque 0.96, human 0.86; gradient angle: marmoset 0.89, macaque 0.82, human 0.96).

(D) Individual genes showing graded expression along the PCg direction. Color scale is min-max normalized per gene within the plotted section. Scale bars represent 2 mm.

(E) Heatmap of binned average gene expression vs. depth along the PCg gradient direction. Each row is normalized, and dots indicate half-maximum bin position.

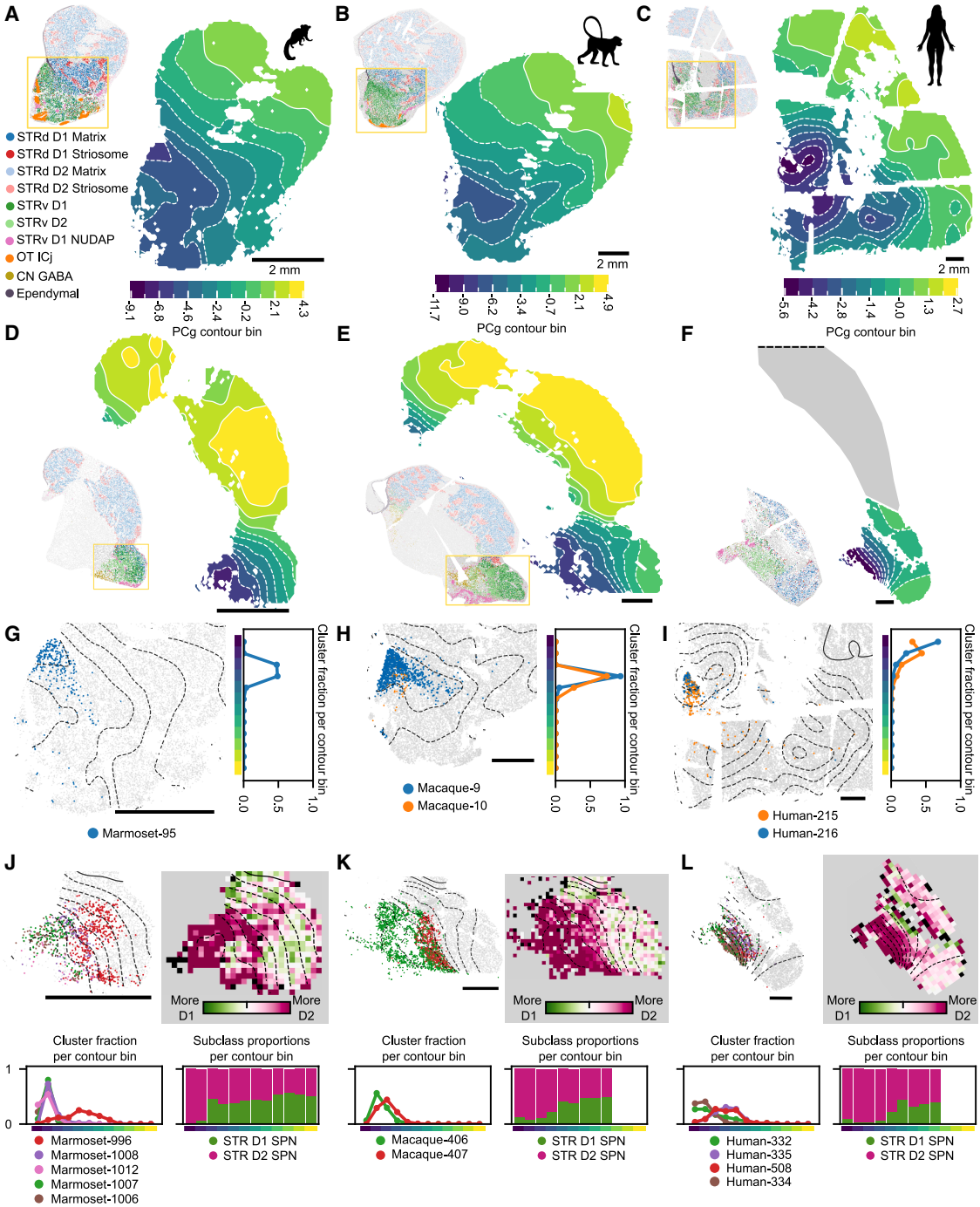


Figure 5. Molecularly distinct subregions in the ventral striatum

(A–C) Contour plots of the gradient principal component (PCg) of rostral striatum sections in marmoset (A), macaque (B), and human (C). Inset, the same section colored by selected cell types. Scale bars represent 2 mm.

(D–F) PCg contour plots of representative caudal striatum sections in marmoset (D), macaque (E), and human (F). In (F), an outline of the approximate location of the putamen is provided to orient the viewer (drawn based on a slab image; a dashed black line indicates where a small portion was cropped out); the human slab-plane is also rotated to better match the expected orientation of the caudate tail in an anatomical reference atlas (see Figures S21D and S21E). Inset, the same section colored by select cell types (the same as in A–C). Scale bars represent 2 mm.

(G–I) SPNs from the subset of the rostral striatum depicted in the insets in (A), (B), and (C). Left, putative NACsmd clusters are highlighted, with other SPNs shown in the background in gray. Contour lines from the corresponding section are overlaid. Right, the fraction of the highlighted clusters found in each contour bin. In all three species, the highlighted clusters are present in an area with low PCg values. Scale bars represent 2 mm.

(legend continued on next page)

with up to five unique clusters per species (Figures S16A–S16D). In each species, two predominant clusters subdivide the STH along its longitudinal axis, with some overlap in the center: Marmoset-1469 (VM-biased) and Marmoset-1470 (DL-biased) (Figure 6B, left); Macaque-474 and Macaque-471 (Figure 6B, center); Human-395 and Human-549 (Figure 6B, right). The dorsal-lateral-biased clusters (Marmoset-1470, Macaque-471, and Human-549) appear to be a conserved *PVALB+* subpopulation found in both primate and mouse.[56–59]

To quantify gene expression variation in the STH, we performed non-spatial PCA on the gene expression of the STH PVALB-PITX2 Glut cells in each species. Two primary axes of spatial variation are observed across primate species: a longitudinal PC that aligns with the VM-DL axis highlighted by the cell-type clusters (Figure 6D, top; Figure 6E), and a transverse PC that varies across both the rostral-caudal axis and the minor (dorsal-medial to ventral-lateral) axis (Figure 6D, bottom). All three species show graded expression of *ADCYAP1* along the longitudinal axis of the STH (Figure 6F), with high expression at the ventral-medial end decreasing to minimal expression at the dorsal-lateral end. *CALB2* exhibits a similar gradient in marmoset and macaque (Figure 6E).

The marker genes that drive this spatial organization are frequently species-specific, which is consistent with previous work that shows cell-type organization can be robustly conserved even in the absence of a fixed set of conserved marker genes.[10,11] We identify species-specific genes that share the major axis high-VM/low-DL gradient pattern (Figures 6C and 6E; Figures S16E and S16F): *SCN9A*, *TNNT1*, *SCN4B*, and *SLIT2* in marmoset and *HTR2C*, *TACR1*, and *GPC5* in macaque. We identified two other organizational differences across the three species. In macaque, a third cluster, Macaque-473, forms a cap at the ventral-medial end of the STH (Figure 6B, center), mirroring projection studies that report distinct properties in the medial tip.[51] Additionally, there is significantly more overlap between the two dominant clusters in human (Figure 6B, right) than in nonhuman primates (NHPs), which is consistent with imaging studies that reported more overlap between functional domains and more inter-individual variation in the human STH.[52,60] Despite these species differences, our spatial atlas suggests that the overall molecular organization of the STH along its longitudinal axis is conserved across primates and shared with rodent.

The primate GPi is organized into a core and shell

The GP is a central hub of the BG that integrates inhibitory and excitatory signals from the STR and STH to regulate motor output and motivational or limbic processing.[61,62] The GP includes the GPi and GPe, each with distinct molecular and functional identities. The GPi is an egg-shaped structure that sits ventral-medial to GPe and has been shown to have central and peripheral regions of cells as defined by their different projection targets.[63,64]

We now show that distinct transcriptomic types in the primate GPi are similarly organized into a core-shell structure (Figures 7A and 7B). Consistent with projection studies,[64] GPi Core GABA cells are more abundant and extend more caudally (Figures 7A and 7B) whereas GPi Shell GABA-Glut cells are more abundant rostrally (Figure 7B, left graphic). In marmoset and macaque, radial histograms of GPi Shell to GPi Core proportions show the transition from core to shell and highlight a ring of higher GPi Shell proportions surrounding a central region of higher GPi Core proportions (Figure 7B, top and middle rows). In human, the GPi Shell is represented by a narrow band of cells primarily between the GPe and GPi with a majority GPi Core-rich area, which likely reflects the extreme caudal location of our limited sampling of this small structure (Figure 7B, bottom row). Marker genes for these cell types show distinct expression profiles (Figure 7C): *MEIS1* and *SLC17A6* are highly expressed in GPi Shell cells while *FOXP2* and *TAFA4* are expressed in GPi Core cells. This marker gene expression is consistent across species in both spatial transcriptomics and snRNA-seq data, demonstrating high conservation of the transcriptomic programs defining the core-shell distinction (Figure 7C, right; Figure S17A). The mouse homolog to GPi, the entopeduncular nucleus, was also recently shown to have a core-shell division in its circuitry, which is mirrored in molecular cell types.[65,66] By integrating publicly available mouse single-cell RNA sequencing (scRNA-seq) and spatial-based taxonomies,[13,41] we identified candidate homologous cell types to our primate GPi Core and GPi Shell (Figure S17B). Indeed, ZI Pax6 Gaba_3 and GPi Tbr1 Cngb3 Gaba-Glut_1 cell types in mouse spatially organize into a core-shell pattern and express marker genes consistent with our findings in primates (Figure S17B).

Primate GPe mirrors rodent molecular organization

In rodent, the GPe is composed of molecularly distinct prototypic and arkypallidal populations,[67] which have phenotypic correlates that have not been transcriptomically confirmed in primate.[68] We find two Groups in all three species, GPe SOX6-CTXND1 GABA and GPe MEIS2-SOX6 GABA (Figures 7A and 7D), which likely correspond to the prototypic and arkypallidal populations, respectively. Consistent with markers for these types in rodent,[67] *LHX6* is highly expressed in GPe SOX6-CTXND1 cells, while *FOXP2* and *MEIS2* are highly expressed in GPe MEIS2-SOX6 cells (Figure 7D; Figure S17C). These GPe cell types are spatially co-mingled but exhibit different proportions in the NHPs compared with human (Figure 7D). In marmoset and macaque, the prototypic-like GPe SOX6-CTXND1 type represents the majority of GPe cells (76% and 70%, respectively), compared with human in which we observe a lower proportion of prototypic-like cells (42%).

(J–L) SPNs from the subset of the caudal striatum depicted in the insets in (D), (E), and (F). Top left, putative AStr clusters are highlighted, with other SPNs shown in the background in gray. Contour lines from the corresponding section are overlaid. Lower left, the fraction of the highlighted clusters found in each contour bin. In all three species, the highlighted clusters are present in an area with low PCg values. Top right, spatial histograms of D1/D2 SPN enrichment (bin sizes: marmoset, 100 μm; macaque, 200 μm; human, 400 μm). Lower right, the proportion of cells belonging to STR D1 SPN or STR D2 SPN Subclasses in each contour bin. Ventral-medial bins, corresponding to the AStr, have more D2 SPNs than D1 SPNs. All scale bars represent 2 mm. Contour bin line plots and stacked bar plots only quantify cells for the sections depicted.

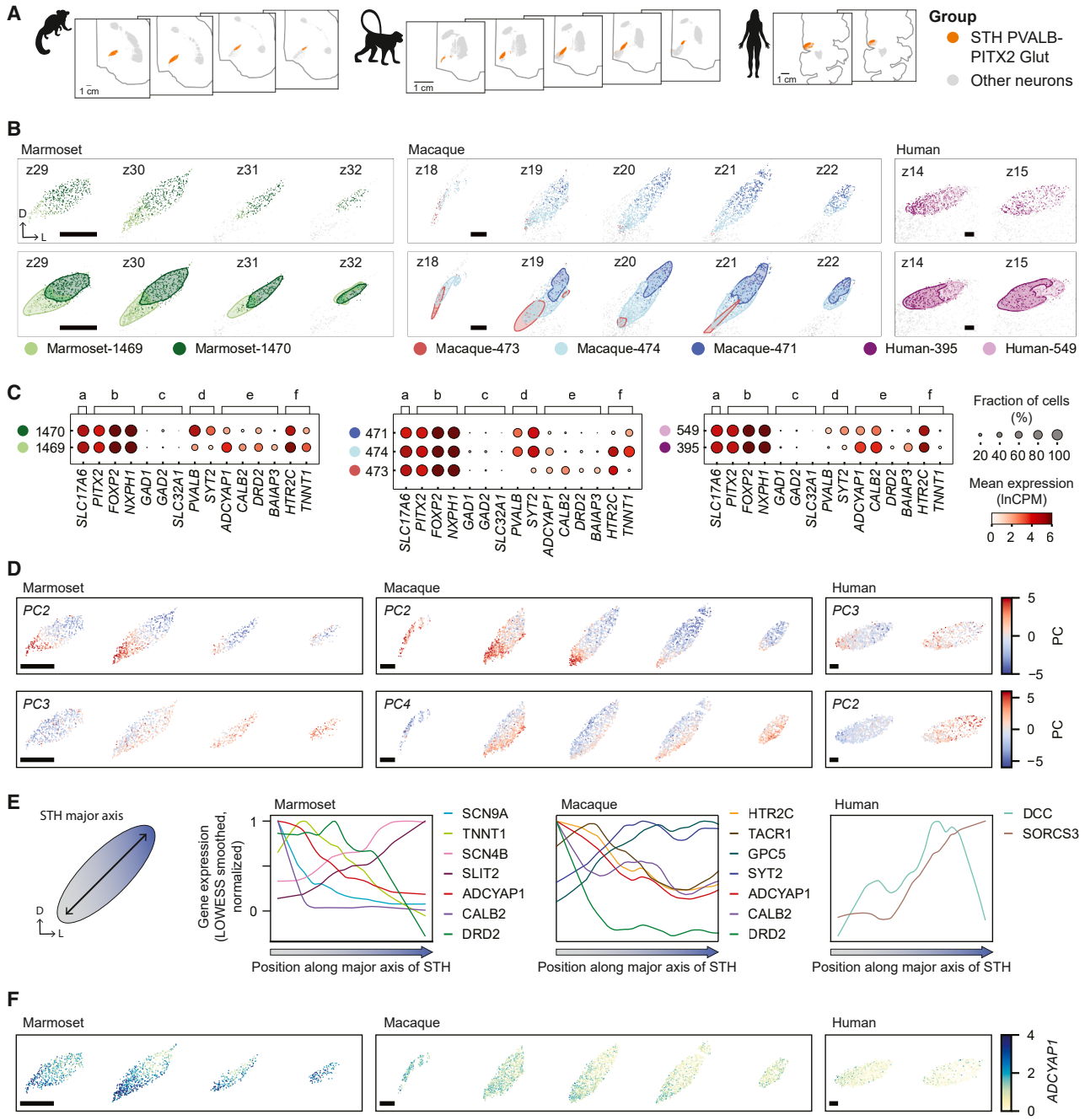


Figure 6. Spatial organization of the subthalamic nucleus

(A) Montage of coronal sections containing the STH, from rostral to caudal, in (left to right) marmoset, macaque, and human, with STH PVALB-PITX2 Glut Group cells in orange and other cells colored gray. Scale bars represent 1 cm.

(B) Dominant clusters in the STH (top) and the kernel density estimate (KDE) contour containing 80% of the cells in each cluster (bottom), showing their biased spatial distribution along the VM-to-DL axis. Scale bars represent 1 mm.

(C) Differential gene expression in the snRNA-seq data for clusters shown in (B).

(D) PCA showing the two axes of spatial variation in each species: longitudinal (top) and transverse plus rostral-caudal (bottom). Scale bars represent 1 mm.

(E) Spatially variable gene expression in each species along the longitudinal, or major, axis of the STH.

(F) In all three species, *ADCYAP1* is high in the VM and low in the DL subthalamic nucleus. Scale bars represent 1 mm.

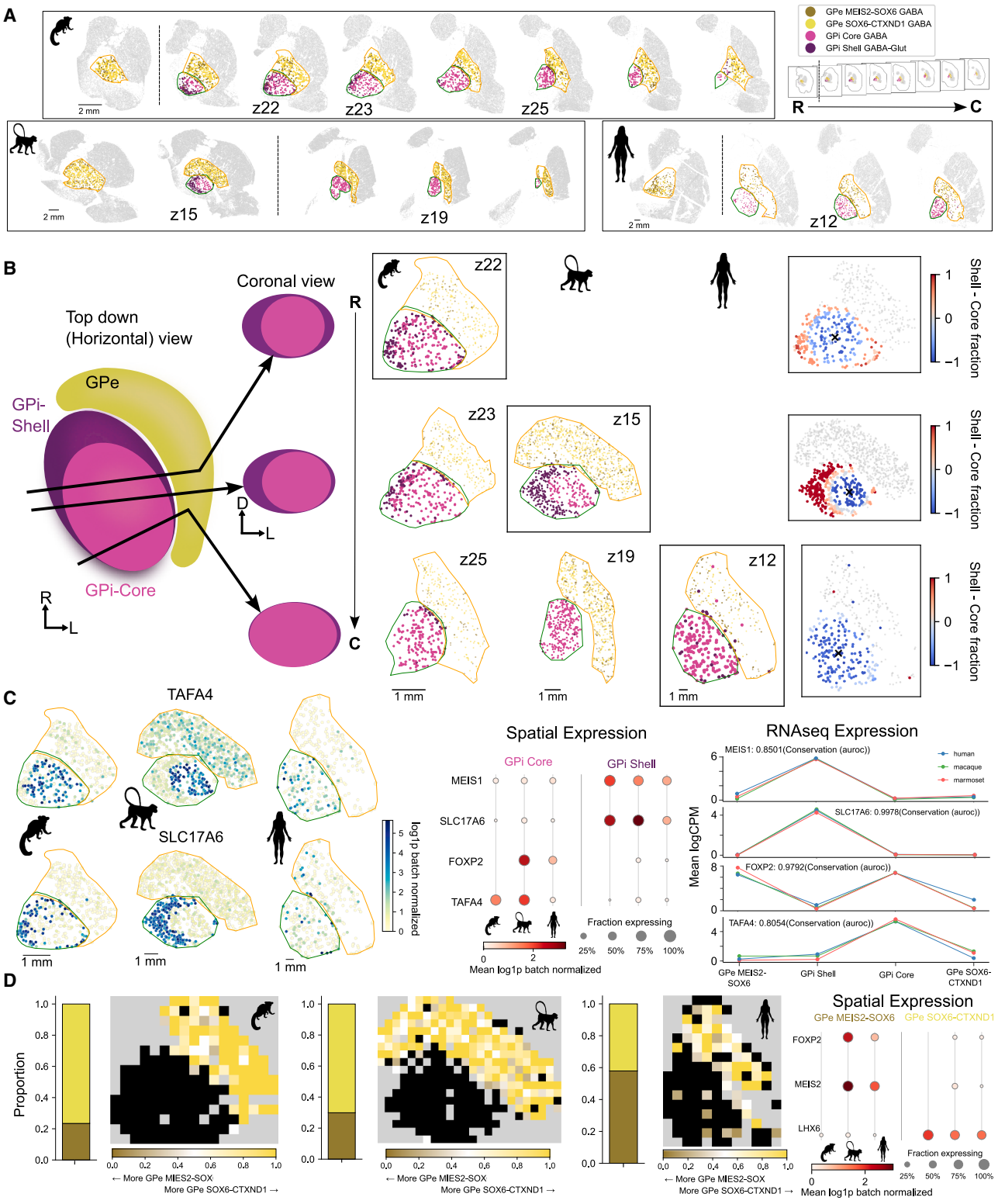


Figure 7. Cell-type localization in the globus pallidus

(A) Montage of coronal sections containing the GP, from rostral to caudal, in each species with GP cells colored by Group and other cells colored gray. Vertical lines indicate breaks between slabs (see STAR Methods). Sections annotated with their z-positions match those in (B, middle). Upper right legend shows the R-C extent in the context of the full hemisphere for marmoset as an example. Scale bars represent 2 mm.

(legend continued on next page)

In mouse GPe, the corresponding prototypic and arkypallidal types are NDB-SI-MA-STRv Lhx8 Gaba_4 and GPe-SI Sox6 Cyp26b1 Gaba_1, respectively, which show similar gene expression patterns and spatial co-mingling to those in NHP and human (Figure S17D). Like NHP species, mouse GPe shows a higher proportion of prototypic-like cells (77% NDB-SI-MA-STRv Lhx8 Gaba_4).

Cross-species BG atlas resources

We have incorporated our spatial transcriptomics atlas into two interactive platforms, the ABC Atlas and Cytosplore, to enable the exploration of BG cell types and gene expression across species. The Allen Institute's ABC Atlas (RRID:SCR_024440) is a web-based platform for visualization of cellular data.[13] The ABC Atlas allows users to view spatial transcriptomics data from all three primate species alongside an integrated cross-species embedding of the snRNA-seq consensus taxonomy, with interactive selection and filtering. Users can also explore cell-type distributions and gene expression across the BG in all three species simultaneously. The data have also been incorporated into the Cytosplore Viewer desktop application[69] and its Gradient Surfer plugin (Figure S18), which offers interactive analyses to compare spatial gene expression gradients across two datasets with partially overlapping gene panels. It is designed to interactively probe for, extract, and align gradient-based gene expression features to identify conserved or divergent molecular patterns related to tissue structure and biological function.

The data used in this paper are available for download alongside tutorials for programmatic access (https://brain-map.org/consortia/hmba/hmba-release-basal-ganglia).

DISCUSSION

The BG are critical components of movement, decision-making, and reward functions in the mammalian brain. Because this system operates through anatomically organized circuits composed of distinct neuronal populations, spatial transcriptomic characterization of these cells is necessary to link molecular cell types to function. With more than one million cells profiled per primate species, sampled from across the full rostral-caudal extent, this spatial atlas is an unprecedented resource for characterizing the molecular organization of the BG. We share this spatial transcriptomics atlas via publicly available data and interactive tools to enable researchers to explore additional pressing scientific questions. By linking species-specific spatial transcriptomics data to a common snRNA-seq reference and multimodal nomenclature, this study provides a more expansive framework for placing BG cells in a shared anatomical and molecular context. We identify the key principles of primate spatial organization while revealing a tension between transcriptomic diversity and anatomical boundaries.

Anatomy vs. molecular identity: It's complicated

The BG were classically characterized through histochemical and anatomical methods, and thus it is tempting to search for clear molecular and cellular delineations between subregions that align with previously characterized domains. The results of our cross-species spatial characterization suggest that the BG involves a complex three-dimensional molecular organization that manifests in multiple axes of variation. These include smooth dorsal-ventral gradients overlaid on discrete forms of molecular identity, such as matrix vs. striosome compartments and D1 vs. D2 identity.

SPNs, the predominant neuronal type of the BG, illustrate this tension between anatomy and molecular identity. Previous studies have not drawn a direct correspondence between SPN subtypes across species or their relationship to anatomical and histochemical divisions of the STR. This is in part because studies performed in a single species,[19,36,70] with limited sampling through rostro-caudal striatal extent, make comprehensive, cross-species comparisons difficult. Our gradient and contour analyses across species show that gene expression gradients cross white matter tracts, such as the internal capsule, and shift across the rostro-caudal axis. Although our sampling does not permit us to reconstruct the direction of this gradient in 3D, the correspondence across 2D sections hints at a 3D gradient that spans anatomical boundaries. This raises the bar for claims that the caudate and putamen are transcriptomically distinct: any apparent difference could depend on where and how sampling is performed. Connectivity patterns and functional output do differ across these structures,[40,71] yet we and others[42,72] find that species-conserved SPN Groups are shared across the caudate and putamen.

The link between anatomy and molecular identity is also complex in the NAC. The NAC is often divided into core (NACc) and shell (NACs) subnuclei, which were found to mediate distinct aspects of stimulus and reward through pharmacological inactivation and lesion studies in rodents.[73–76] Histochemically, these subnuclei have been distinguished using differential calbindin expression (*CALB1*), with NACs identified as "calbindin-poor" in contrast to the "calbindin-rich" NACc.[35,77,78] However,

(B) Left shows a diagram of the GPe and GPi as viewed top-down (horizontal view) with black lines indicating the approximate slice plane that would result in different coronal views of the GPi core and shell. The middle highlights these views in spatial data from each species organized in columns. All three views are captured in marmoset, two in macaque, and one in human. At the right are radial histograms of GPi Core and GPi Shell Groups projected into spatial coordinates for the boxed section in the middle panel. The center of the histogram is denoted by an "X" and the bin size (in microns) for marmoset is 100, macaque 200, and human 600. Scale bars represent 1 mm.

(C) Left and middle show the gene expression of *TAFA4* and *SLC17A6*; marker genes for GPi Core and Shell, respectively, are shown in spatial coordinates and as expression dot plots. Right shows expressolog plots of marker genes from snRNA-seq data (full expressologs are shown in Figure S17A and S17C). Scale bars represent 1 mm.

(D) Proportion and spatial histogram of GPe MEIS2-SOX6 GABA and GPe SOX6-CTXND1 GABA Groups in the GPe. Yellow/brown areas are the fraction of each Group in each bin on a diverging color scale, while black bins do not contain either of these Groups. Bin size (in microns) for marmoset is 200, macaque 350, and human 800. Far right shows expression dot plots of marker genes.

in primates, this pattern is inconsistent across species and the rostral-caudal axis, and a sharp boundary between calbindin-poor NACs and calbindin-rich NACc is not always visible (Figure S14G).[49] Similarly, transcriptomic cell types specific to NACc and NACs have been reported in mouse,[41] but our spatial analysis did not find conserved Groups that robustly delineate NACc from NACs in primates, consistent with findings in macaque.[19] Furthermore, the lack of a definite anatomical boundary in this region in primates makes it challenging to identify clusters or gene expression patterns specific to these subregions. Therefore, the relationship between molecular features and known functional domains remains unclear in the STRv and will require developmental or cross-modal functional assessment for clarification.

Graded molecular organization mirrors graded connectivity

The interplay between molecular identities and functional circuits of the BG is a rich and ongoing area of research. The discrete molecular dichotomies of striosome-matrix and D1-D2 organization in the STR have recently been shown to reflect antiparallel functional streams in mouse, with striosomes containing their own direct and indirect pathways that oppose those in the matrix.[79] At the same time, corticostriatal projections are organized along a ventral-medial to dorsal-lateral axis, with an associative region forming a transition zone between a dorsal-lateral motor region and a ventral-medial limbic tip.[4] Exploration of circuit function in these regions includes fMRI methods. Some fMRI analyses use clustering approaches that emphasize a more discrete organization of the STR,[52,80–82] which is practical for comparing across species, modalities, or datasets but can also obscure subtle details of the underlying gradients.[83,84] Notably, when other studies have applied non-discretizing analysis methods, they resolve connectivity data into multiple overlapping topographies[81,85] that are strikingly consistent with the gene expression gradients captured by PCg.

A parallel topographic organization has been identified in the STH, an important clinical target for deep brain stimulation in the treatment of motor symptoms of Parkinson's disease, with overlapping functional domains along its longitudinal axis.[51,52,86,87] Recent studies in mouse and macaque show that the molecular organization of the STH parallels these topographical gradients of connectivity, and our data extend this observation across primate species.[53–56]

We also find evidence that striatal gene expression gradients extend into adjacent regions. Previous histochemical and tracing studies have identified the NACsmd and AStr as transition zones with their neighboring striatal-like extended amygdala regions in both rodent and primate.[46,88,89] Our study now shows that NACsmd and AStr serve as ventral anchor points of a striatal gene gradient in the rostral and caudal STR. We also identify unique clusters and gene expression in the NACsmd and AStr, suggesting molecular specialization of SPNs in these regions across primate species, although this did not rise to the level of a conserved Group. Our AStr clusters are D2 positive and may be homologous to AStr D2 SPNs in mouse, which have been shown to have specific functions in negative valence.[50] The functional role of D1 SPNs in the NACsmd is less clear, although we note that the spatial distribution of our NACsmd-specific clusters resembles that of localized projections in macaque, which are restricted to this region of the NACs.[89]

Although our spatial transcriptomics data alone cannot establish a link between molecular characteristics and connectivity or functional data, the resemblance is striking. Future studies integrating spatial transcriptomics data with projection data could investigate the link between molecular specialization and connectivity more directly.

Primate analog of GPi core-shell and striatal exo-patch cell types

In the GP, we uncovered a molecular organization in the primate BG that had previously been described only in rodent. Our spatial data show that the GPi is organized into a core and shell, each dominated by its own, conserved transcriptomic cell type. The primate GPi is homologous to the mouse entopeduncular nucleus, which was recently shown to have molecularly distinct core and shell divisions that are differentially innervated by striatal/pallidal sources and that route output to distinct downstream targets.[65,66,90,91] Prior axon tracing work in primates hinted at a similar spatial pattern of projections in the GPi but did not characterize the molecular identities of the cells present.[63,64,92] Our spatial atlas now describes transcriptomic cell types associated with the GPi core and shell.

Additionally, we find transcriptomic evidence of a small population of cells with strong striosome-like gene expression that resides far away from striosome compartment masks in the same two-dimensional plane. These cells may be a primate analog to mouse "exo-patch" cells, which are scattered throughout the matrix but molecularly and developmentally resemble striosome SPNs.[93–95] Cementing these striosome-like cells as a conserved, biologically relevant population in primates will require further studies to investigate their developmental origin, projection patterns, functional properties, and precise localization relative to the complex 3D lattice of striosomes. These follow-up studies will be particularly intriguing because recent work has shown that SPNs in striosome and matrix compartments have distinct connectivity patterns with opposite effects on motor function.[79] This raises the question: do these striosome-like cells in the matrix participate in striosome circuits or matrix circuits? In other words, do they obey their cell type or compartment identity in primates?

Limitations of the study

Although this study represents comprehensive sampling across the full rostral-caudal extent of the BG nuclei, our spatial transcriptomics data collection was limited to a single donor hemisphere per primate species. Thus, this resource is not situated to address questions of inter-individual variation, sexual dimorphism, or hemispheric lateralization. Further, additional donors of all species will be needed to confirm the cross-species conservation of spatial organization. Additionally, the imaging-based platforms available at the time of data collection limited us to 300 genes per species and a tiled sampling strategy in the larger macaque and human brains. Future spatial atlases of the primate brain will be able to take

advantage of emerging platforms that can image thousands of genes in a larger imaging area. Data processing and analysis methods for spatial transcriptomics are also still maturing. For instance, cell segmentation is considered an outstanding challenge in both spatial transcriptomics and the wider microscopy field.[96] Although this study took advantage of available improvements in cell staining techniques and deep learning-augmented algorithms,[97] work is ongoing to account for transcript spillover and unsegmented transcripts outside of cell bodies.[98–100] Similarly, algorithms for label transfer from single-cell reference datasets to spatial cells are an area of active development, with work focused on better accounting for gaps in the reference data and technical differences in transcript measurements between these two modalities. Future spatial atlases will benefit from ongoing efforts to improve, optimize, and benchmark these computational methods.

Toward whole-brain primate atlases

The BRAIN Initiative Cell Atlas Network (BICAN; RRID:SCR_022794) is a collaboration among neuroscientists to create comprehensive, multimodal, whole-brain atlases of the NHP and human brains. We created a spatial transcriptomics atlas that provides a framework for integrating spatial and molecular cellular features. These efforts in the BG yielded important outcomes that we will extend to whole-brain efforts. First, we based this atlas on a cross-species, cross-modal cell-type taxonomy, with cell-type nomenclature informed by single-nucleus transcriptomics, spatial transcriptomics, and patch-seq methodologies. Second, we grounded the spatial transcriptomics atlas in the anatomy by referencing existing neuroanatomical atlases and ensuring that structures were sampled multiple times and across anatomical boundaries. This allowed us to capture transition areas and understand the full extent of larger spatial organization, which will only be more important in a whole-brain context.

RESOURCE AVAILABILITY

Lead contact

Further information and requests for resources and reagents should be direct to and will be fulfilled by the lead contact, Stephanie C. Seeman (stephanies@alleninstitute.org).

Materials availability

This study did not generate any new, unique reagents.

Data and code availability

- Spatial transcriptomics data have been deposited at the Brain Image Library (BIL: 10.35077/g.1211) and are publicly available as of the date of publication.
- All original code has been deposited at GitHub (https://github.com/AllenInstitute/BG_HMBA_Spatial) and is publicly available as of the date of publication.
- Any additional information required to reanalyze the data reported in this paper is available from the lead contact upon request.

ACKNOWLEDGMENTS

We thank Song-Lin Ding for conversations on anatomical delineations, the BG Analysis Working Group for discussions around cell typing, and Chelsea Pagan for program management support. We also thank Cliff Slaughterbeck and the SIPE team for instrumentation and software support. We thank Raymond Sanchez, Elysha Fiabane, Chris Morrison, Scott Daniel, and Tyler Mollenkopf of the Data and Technology team for product development. We thank the animal care personnel and veterinary staff at the MIT DCM and Rockefeller for their dedicated help with animal husbandry and expert clinical support. The authors thank the Allen Institute founder Paul G. Allen, for his vision, encouragement, and support, and Allen Institute chair Jody Allen. This publication was supported by and coordinated through the Brain Initiative Cell Atlas Network (BICAN). Research reported in this publication was funded by the National Institute of Mental Health under NIH award UM1MH130981-01 and the Allen Institute for Brain Science.

AUTHOR CONTRIBUTIONS

Conceptualization: M.N.H., M.A.T., N.J., D.A.M., Z.M.M., F.M.K., T.E.B., R.D.H., L.N., J.L.C., B. Long, and S.C.S.; data curation: M.N.H., M.A.T., N.J., D.A.M., A.R., M.H., S. Barta, N.M., N.V.C., P.O., J.N., J.C., M.M.V., S.R., Z.J., S.H., T. Hayashi, Z.M.M., C.D.K., J.A., J.W., R.D.H., J.L.C., B. Long, and S.C.S.; formal analysis: M.N.H., M.A.T., N.J., S.D., M.D., Y.F., I.K., F.Y., B.Q.R., M.F.G., T. Hayashi, O.K., C.D.K., D.C.V.E., J.L.C., B. Long, and S.C.S.; funding acquisition: T. Hayashi, T.J., W.F., D.C.V.E., F.M.K., T.E.B., R.D.H., H.Z., E.S.L., J.L.C., and B. Long; investigation: M.N.H., M.A.T., D.A.M., A.R., S. Barta, N.M., N.V.C., P.O., J.N., J.C., M.M.V., S.R., Z.J., F.Y., K.L., W.F., R.D.H., J.L.C., B. Long, and S.C.S.; methodology: M.N.H., M.A.T., A.D.G., O.K., J.L.C., B. Long, and S.C.S.; project administration: L.K., C.D.K., F.M.K., H.Z., E.S.L., J.L.C., B. Long, and S.C.S.; resources: F.Y., Q.Z., K.L., G.F., T. Hayashi, W.F., C.D.K., and F.M.K.; software: M.N.H., M.A.T., M.H., J.Q., L. Ching, S. Basu, T. Höllt, C.L., B. Lelieveldt, F.Y., B.Q.R., O.K., L. Campagnola, T.J., L.N., B. Long, and S.C.S.; supervision: M.K., B. Lelieveldt, M.F.G., L.K., W.F., C.D.K., D.C.V.E., J.A., J.W., F.M.K., T.E.B., R.D.H., L.N., H.Z., E.S.L., J.L.C., B. Long, and S.C.S.; validation: M.N.H., M.A.T., B. Long, and S.C.S.; visualization: M.N.H., M.A.T., M.H., S. Basu, T. Höllt, C.L., B. Lelieveldt, L.N., B. Long, and S.C.S.; writing – original draft: M.N.H., M.A.T., D.A.M., M.H., S. Basu, B. Lelieveldt, J.L.C., B. Long, and S.C.S.; writing – review & editing: M.N.H., M.A.T., N.J., M.F.G., B.Q.R., D.C.V.E., J.W., F.M.K., T.E.B., H.Z., E.S.L., J.L.C., B. Long, and S.C.S.

DECLARATION OF INTERESTS

H.Z. is on the scientific advisory board of MapLight Therapeutics, Inc.

DECLARATION OF GENERATIVE AI AND AI-ASSISTED TECHNOLOGIES IN THE MANUSCRIPT PREPARATION PROCESS

During the preparation of this work, the authors used OpenAI ChatGPT, Anthropic Claude, and Microsoft Copilot to assist in a subset of coding tasks for figure generation and literature searches. The authors fully reviewed and edited all AI-generated content and take full responsibility for the content in this publication.

STAR★METHODS

Detailed methods are provided in the online version of this paper and include the following:

- KEY RESOURCES TABLE
- EXPERIMENTAL MODEL AND STUDY PARTICPANT DETAILS
  - Human
  - Macaque
  - Marmoset
- METHOD DETAILS
  - Tissue processing
  - Gene panel design
  - Spatial transcriptomics data acquisition
  - Spatial data post-processing
  - Section and block alignment
  - Manual anatomical annotations

- Anatomical orientation across species to reference atlases
- QUANTIFICATION AND STATISTICAL ANALYSIS
  - Normalization
  - Spatial domain detection
  - Cell type mapping
  - Data inclusion criteria
  - Compartment masks
  - Cell type enrichment in compartments
  - MetaNeighbor
  - Calculation of distance to nearest striosome compartment
  - Striosome versus Matrix SPN scores
  - Candidate striosome-like cell inclusion criteria
  - Principal component analysis (PCA) and gradient analysis
  - Contour plots
  - DEG dot plots
  - Mouse data
  - Cytosplore Gradient Surfer
- ADDITIONAL RESOURCES

SUPPLEMENTAL INFORMATION

Supplemental information can be found online at https://doi.org/10.1016/j.cell.2026.10.023.

Received: November 24, 2025
Revised: August 29, 2026
Accepted: October 14, 2026
Published: November 12, 2026

REFERENCES

1. Haber, S.N., Adler, A., and Bergman, H. (2012). The Basal GangliaChapter 20. In The Human Nervous System, Third Edition (Elsevier), pp. 678–738. https://doi.org/10.1016/B978-0-12-374236-0.10020-3.
2. Albin, R.L., Young, A.B., and Penney, J.B. (1989). The functional anatomy of basal ganglia disorders. Trends Neurosci. *12*, 366–375. https://doi.org/10.1016/0166-2236(89)90074-x.
3. Parent, M., and Parent, A. (2010). Substantia nigra and Parkinson's disease: a brief history of their long and intimate relationship. Can. J. Neurol. Sci. *37*, 313–319. https://doi.org/10.1017/s0317167100010209.
4. Fudge, J.L., and Haber, S.N. (2002). Defining the Caudal Ventral Striatum in Primates: Cellular and Histochemical Features. J. Neurosci. *22*, 10078–10082. https://doi.org/10.1523/JNEUROSCI.22-23-10078.2002.
5. Haber, S.N. (2016). Corticostriatal circuitry. Dial. Clin. Neurosci. *18*, 7–21. https://doi.org/10.31887/DCNS.2016.18.1/shaber.
6. Hirter, K.N., Miller, E.N., Stimpson, C.D., Phillips, K.A., Hopkins, W.D., Hof, P.R., Sherwood, C.C., Lovejoy, C.O., and Raghanti, M.A. (2021). The nucleus accumbens and ventral pallidum exhibit greater dopaminergic innervation in humans compared to other primates. Brain Struct. Funct. *226*, 1909–1923. https://doi.org/10.1007/s00429-021-02300-0.
7. Hunnicutt, B.J., Jongbloets, B.C., Birdsong, W.T., Gertz, K.J., Zhong, H., and Mao, T. (2016). A comprehensive excitatory input map of the striatum reveals novel functional organization. eLife *5*, e19103. https://doi.org/10.7554/eLife.19103.
8. Parent, A., Fortin, M., Côté, P.Y., and Cicchetti, F. (1996). Calcium-binding proteins in primate basal ganglia. Neurosci. Res. *25*, 309–334. https://doi.org/10.1016/0168-0102(96)01065-6.
9. Prensa, L., Richard, S., and Parent, A. (2003). Chemical anatomy of the human ventral striatum and adjacent basal forebrain structures. J. Comp. Neurol. *460*, 345–367. https://doi.org/10.1002/cne.10627.
10. Arendt, D., Musser, J.M., Baker, C.V.H., Bergman, A., Cepko, C., Erwin, D.H., Pavlicev, M., Schlosser, G., Widder, S., Laubichler, M.D., et al. (2016). The origin and evolution of cell types. Nat. Rev. Genet. *17*, 744–757. https://doi.org/10.1038/nrg.2016.127.
11. Bakken, T.E., Jorstad, N.L., Hu, Q., Lake, B.B., Tian, W., Kalmbach, B.E., Crow, M., Hodge, R.D., Krienen, F.M., Sorensen, S.A., et al. (2021). Comparative cellular analysis of motor cortex in human, marmoset and mouse. Nature *598*, 111–119. https://doi.org/10.1038/s41586-021-03465-8.
12. Siletti, K., Hodge, R., Mossi Albiach, A., Lee, K.W., Ding, S.-L., Hu, L., Lönnerberg, P., Bakken, T., Casper, T., Clark, M., et al. (2023). Transcriptomic diversity of cell types across the adult human brain. Science *382*, eadd7046. https://doi.org/10.1126/science.add7046.
13. Yao, Z., Van Velthoven, C.T.J., Kunst, M., Zhang, M., McMillen, D., Lee, C., Jung, W., Goldy, J., Abdelhak, A., Aitken, M., et al. (2023). A high-resolution transcriptomic and spatial atlas of cell types in the whole mouse brain. Nature *624*, 317–332. https://doi.org/10.1038/s41586-023-06812-z.
14. Yuste, R., Hawrylycz, M., Aalling, N., Aguilar-Valles, A., Arendt, D., Armañanzas, R., Ascoli, G.A., Bielza, C., Bokharaie, V., Bergmann, T.B., et al. (2020). A community-based transcriptomics classification and nomenclature of neocortical cell types. Nat. Neurosci. *23*, 1456–1468. https://doi.org/10.1038/s41593-020-0685-8.
15. Zeng, H., and Sanes, J.R. (2017). Neuronal cell-type classification: challenges, opportunities and the path forward. Nat. Rev. Neurosci. *18*, 530–546. https://doi.org/10.1038/nrn.2017.85.
16. Hodge, R.D., Bakken, T.E., Miller, J.A., Smith, K.A., Barkan, E.R., Graybuck, L.T., Close, J.L., Long, B., Johansen, N., Penn, O., et al. (2019). Conserved cell types with divergent features in human versus mouse cortex. Nature *573*, 61–68. https://doi.org/10.1038/s41586-019-1506-7.
17. Jorstad, N.L., Close, J., Johansen, N., Yanny, A.M., Barkan, E.R., Travaglini, K.J., Bertagnolli, D., Campos, J., Casper, T., Crichton, K., et al. (2023). Transcriptomic cytoarchitecture reveals principles of human neocortex organization. Science *382*, eadf6812. https://doi.org/10.1126/science.adf6812.
18. Jorstad, N.L., Song, J.H.T., Exposito-Alonso, D., Suresh, H., Castro-Pacheco, N., Krienen, F.M., Yanny, A.M., Close, J., Gelfand, E., Long, B., et al. (2023). Comparative transcriptomics reveals human-specific cortical features. Science *382*, eade9516. https://doi.org/10.1126/science.ade9516.
19. He, J., Kleyman, M., Chen, J., Alikaya, A., Rothenhoefer, K.M., Ozturk, B.E., Wirthlin, M., Bostan, A.C., Fish, K., Byrne, L.C., et al. (2021). Transcriptional and anatomical diversity of medium spiny neurons in the primate striatum. Curr. Biol. *31*, 5473–5486.e6. https://doi.org/10.1016/j.cub.2021.10.015.
20. Krienen, F.M., Levandowski, K.M., Zaniewski, H., Del Rosario, R.C.H., Schroeder, M.E., Goldman, M., Wienisch, M., Lutservitz, A., Beja-Glasser, V.F., Chen, C., et al. (2023). A marmoset brain cell census reveals regional specialization of cellular identities. Sci. Adv. *9*, eadk3986. https://doi.org/10.1126/sciadv.adk3986.
21. Johansen, N.J., Fu, Y., Schmitz, M., Dubuc, A., Kempynck, N., Wirthlin, M., Garcia, A.D., Hewitt, M., Turner, M.A., Seeman, S.C., et al. (2026). Cross-species consensus atlas of the primate basal ganglia. Cell. *189*, 7309–7329.e13. https://doi.org/10.1016/j.cell.2026.10.012.
22. Liu, X.-P., Dalley, R., Johansen, N., Budzillo, A., Thijssen, J., Miller, J.A., Walling-Bell, S., Sawchuk, S., Waleboer, F., Alfiler, L., et al. (2026). Morphoelectric diversity and specialization of primate striatal neuron types. Cell *189*, 7492–7511.e9. https://doi.org/10.1016/j.cell.2026.10.028.
23. Ding, S.-L., Bhandiwad, A.A., Rosen, B.Q., Seeman, S.C., Long, B., Johansen, N.J., Bayindir, U., Facer, B., Fu, Y., Halimi, Y., et al. (2026). Harmonized brain ontology and 3D atlases for human, macaque, and marmoset basal ganglia. Cell. *189*, 7616–7633.e7. https://doi.org/10.1016/j.cell.2026.10.033.
24. Lemos, J.C., Duhne, M., and Chuhma, N. (2026). Regional heterogeneity of striatal cholinergic interneurons: setting the stage for diverse behavioral repertoires. Front. Cell. Neurosci. *20*, 1718947. https://doi.org/10.3389/fncel.2026.1718947.

25. Chen, R., Blosser, T.R., Djekidel, M.N., Hao, J., Bhattacherjee, A., Chen, W., Tuesta, L.M., Zhuang, X., and Zhang, Y. (2021). Decoding molecular and cellular heterogeneity of mouse nucleus accumbens. Nat. Neurosci. *24*, 1757–1771. https://doi.org/10.1038/s41593-021-00938-x.

26. Garma, L.D., Harder, L., Barba-Reyes, J.M., Marco Salas, S., Díez-Salguero, M., Nilsson, M., Serrano-Pozo, A., Hyman, B.T., and Muñoz-Manchado, A.B. (2024). Interneuron diversity in the human dorsal striatum. Nat. Commun. *15*, 6164. https://doi.org/10.1038/s41467-024-50414-w.

27. Eid, L., Parent, A., and Parent, M. (2016). Asynaptic feature and heterogeneous distribution of the cholinergic innervation of the globus pallidus in primates. Brain Struct. Funct. *221*, 1139–1155. https://doi.org/10.1007/s00429-014-0960-0.

28. Mesulam, M.M., and Geula, C. (1988). Nucleus basalis (Ch4) and cortical cholinergic innervation in the human brain: Observations based on the distribution of acetylcholinesterase and choline acetyltransferase. J. Comp. Neurol. *275*, 216–240. https://doi.org/10.1002/cne.902750205.

29. Mesulam, M.M., Mufson, E.J., Levey, A.I., and Wainer, B.H. (1983). Cholinergic innervation of cortex by the basal forebrain: Cytochemistry and cortical connections of the septal area, diagonal band nuclei, nucleus basalis (substantia innominata), and hypothalamus in the rhesus monkey. J. Comp. Neurol. *214*, 170–197. https://doi.org/10.1002/cne.902140206.

30. Barba-Reyes, J.M., Harder, L., Marco Salas, S., Jaisa-Aad, M., Muñoz-Castro, C., Garma, L.D., Rafati, N., Nilsson, M., Hyman, B.T., Serrano-Pozo, A., et al. (2025). Oligodendroglia vulnerability in the human dorsal striatum in Parkinson's disease. Acta Neuropathol. *149*, 46. https://doi.org/10.1007/s00401-025-02884-5.

31. Yuan, G., Suresh, V., Wigdor, E., Hao, Y., Leonard, R., Steyert, M., Griffiths, M., Evans, C., Rohani, N., Weiss, J., et al. (2026). Disruption of Cell-Type-Specific Molecular Programs of Medium Spiny Neurons in Autism. Cell *189*, 7528–7549.e15. https://doi.org/10.1016/j.cell.2026.10.027.

32. Fu, Y., Kempynck, N., Ding, W., Turner, M.A., Garcia, A.D., Schmitz, M.T., Close, J., Kapen, I., Hewitt, M., Seeman, S.C., et al. (2026). Circuit-aligned specialization of human basal ganglia astrocytes. Cell *189*, 7512–7527.e6. https://doi.org/10.1016/j.cell.2026.09.041.

33. Dan, S., Turner, M.A., Long, B., and Krienen, F.M. (2026). Spatial patterning of transcriptional and regulatory programs in the primate subcortex. Cell *189*, 7471–7491.e10. https://doi.org/10.1016/j.cell.2026.10.007.

34. Graybiel, A.M., and Ragsdale, C.W., Jr. (1978). Histochemically distinct compartments in the striatum of human, monkeys, and cat demonstrated by acetylthiocholinesterase staining. Proc. Natl. Acad. Sci. USA *75*, 5723–5726. https://doi.org/10.1073/pnas.75.11.5723.

35. Voorn, P., Brady, L.S., Berendse, H.W., and Richfield, E.K. (1996). Densitometrical analysis of opioid receptor ligand binding in the human striatum—I. Distribution of μ opioid receptor defines shell and core of the ventral striatum. Neuroscience *75*, 777–792. https://doi.org/10.1016/0306-4522(96)00271-0.

36. Stanley, G., Gokce, O., Malenka, R.C., Südhof, T.C., and Quake, S.R. (2020). Continuous and Discrete Neuron Types of the Adult Murine Striatum. Neuron *105*, 688–699.e8. https://doi.org/10.1016/j.neuron.2019.11.004.

37. Meyer, G., Gonzalez-Hernandez, T., Carrillo-Padilla, F., and Ferres-Torres, R. (1989). Aggregations of granule cells in the basal forebrain (islands of Calleja): Golgi and cytoarchitectonic study in different mammals, including man. J. Comp. Neurol. *284*, 405–428. https://doi.org/10.1002/cne.902840308.

38. Mikula, S., Parrish, S.K., Trimmer, J.S., and Jones, E.G. (2009). Complete 3D visualization of primate striosomes by KChIP1 immunostaining. J. Comp. Neurol. *514*, 507–517. https://doi.org/10.1002/cne.22051.

39. Goto, S., Kawarai, T., Morigaki, R., Okita, S., Koizumi, H., Nagahiro, S., Munoz, E.L., Lee, L.V., and Kaji, R. (2013). Defects in the striatal neuropeptide Y system in X-linked dystonia-parkinsonism. Brain *136*, 1555–1567. https://doi.org/10.1093/brain/awt084.

40. Selemon, L.D., and Goldman-Rakic, P.S. (1985). Longitudinal topography and interdigitation of corticostriatal projections in the rhesus monkey. J. Neurosci. *5*, 776–794. https://doi.org/10.1523/JNEUROSCI.05-03-00776.1985.

41. Van Velthoven, C.T.J., Gao, Y., Kunst, M., Lee, C., McMillen, D., Chakka, A.B., Casper, T., Clark, M., Chakrabarty, R., Daniel, S., et al. (2025). Transcriptomic and spatial organization of telencephalic GABAergic neurons. Nature *647*, 143–156. https://doi.org/10.1038/s41586-025-09296-1.

42. Berackey, B.T., Tan, Z., Wu, G., Das, S.C., Li, R., Esser, B., Ye, Q., Nafisi, M., Park, S.S., Mendieta, P.A.S., et al. (2026). Multiscale Spatial Transcriptomic Atlas of Human Basal Ganglia Cell-Type and Cellular Community Organization. Cell *189*, 7428–7446.e11. https://doi.org/10.1016/j.cell.2026.09.027.

43. Firestein, B.L., Firestein, B.L., Brenman, J.E., Aoki, C., Sanchez-Perez, A.M., El-Husseini, A.E., and Bredt, D.S. (1999). Cypin: A Cytosolic Regulator of PSD-95 Postsynaptic Targeting. Neuron *24*, 659–672. https://doi.org/10.1016/S0896-6273(00)81120-4.

44. Liang, J., Lyu, J., Zhao, M., Li, D., Zheng, M., Fang, Y., Zhao, F., Lou, J., Guo, C., Wang, L., et al. (2017). Tespa1 regulates T cell receptor-induced calcium signals by recruiting inositol 1,4,5-trisphosphate receptors. Nat. Commun. *8*, 15732. https://doi.org/10.1038/ncomms15732.

45. Haber, S.N., and McFarland, N.R. (1999). The Concept of the Ventral Striatum in Nonhuman Primates. Ann. N. Y. Acad. Sci. *877*, 33–48. https://doi.org/10.1111/j.1749-6632.1999.tb09259.x.

46. deCampo, D.M., and Fudge, J.L. (2013). Amygdala projections to the lateral bed nucleus of the stria terminalis in the macaque: Comparison with ventral striatal afferents. J. Comp. Neurol. *521*, 3191–3216. https://doi.org/10.1002/cne.23340.

47. Ito, R., Robbins, T.W., Pennartz, C.M., and Everitt, B.J. (2008). Functional interaction between the hippocampus and nucleus accumbens shell is necessary for the acquisition of appetitive spatial context conditioning. J. Neurosci. *28*, 6950–6959. https://doi.org/10.1523/JNEUROSCI.1615-08.2008.

48. Marinescu, A.-M., Kamal, E., Leary, P., Navarro I Batista, K., Klug, M., Savić, N., Le Foll, C., and Labouesse, M.A. (2026). The nucleus accumbens shell regulates hedonic feeding via a rostral hotspot. eLife *14*, RP108639. https://doi.org/10.7554/eLife.108639.

49. Meredith, G.E., Pattiselanno, A., Groenewegen, H.J., and Haber, S.N. (1996). Shell and core in monkey and human nucleus accumbens identified with antibodies to calbindin-D28k. J. Comp. Neurol. *365*, 628–639. https://doi.org/10.1002/(SICI)1096-9861(19960219)365:4<628::AID-CNE9>3.0.CO;2-6.

50. Mills, F., Lee, C.R., Howe, J.R., Li, H., Shao, S., Keisler, M.N., Lemieux, M.E., Taschbach, F.H., Keyes, L.R., Borio, M., et al. (2026). Amygdalostriatal transition zone neurons encode sustained cue responses to guide defensive behaviors. Neuron *115*. https://doi.org/10.1016/j.neuron.2026.08.012.

51. Haynes, W.I.A., and Haber, S.N. (2013). The Organization of Prefrontal-Subthalamic Inputs in Primates Provides an Anatomical Substrate for Both Functional Specificity and Integration: Implications for Basal Ganglia Models and Deep Brain Stimulation. J. Neurosci. *33*, 4804–4814. https://doi.org/10.1523/JNEUROSCI.4674-12.2013.

52. Lambert, C., Zrinzo, L., Nagy, Z., Lutti, A., Hariz, M., Foltynie, T., Draganski, B., Ashburner, J., and Frackowiak, R. (2012). Confirmation of functional zones within the human subthalamic nucleus: Patterns of connectivity and sub-parcellation using diffusion weighted imaging. NeuroImage *60*, 83–94. https://doi.org/10.1016/j.neuroimage.2011.11.082.

53. Dumas, S., Francois, C., Karachi, C., and Wallén-Mackenzie, Å. (2025). Spatio-molecular analysis of primate subthalamus defines anatomical domains relevant to Parkinson's disease and neuropsychiatry. Preprint at bioRxiv. https://doi.org/10.1101/2025.05.21.655268.

54. Emmi, A., Campagnolo, M., Stocco, E., Carecchio, M., Macchi, V., Antonini, A., De Caro, R., and Porzionato, A. (2023). Neurotransmitter and

receptor systems in the subthalamic nucleus. Brain Struct. Funct. *228*, 1595–1617. https://doi.org/10.1007/s00429-023-02678-z.

55. Jeon, H., Lee, H., Kwon, D.-H., Kim, J., Tanaka-Yamamoto, K., Yook, J.S., Feng, L., Park, H.R., Lim, Y.H., Cho, Z.-H., et al. (2022). Topographic connectivity and cellular profiling reveal detailed input pathways and functionally distinct cell types in the subthalamic nucleus. Cell Rep. *38*, 110439. https://doi.org/10.1016/j.celrep.2022.110439.

56. Wallén-Mackenzie, Å., Dumas, S., Papathanou, M., Martis Thiele, M.M., Vlcek, B., König, N., and Björklund, Å.K. (2020). Spatio-molecular domains identified in the mouse subthalamic nucleus and neighboring glutamatergic and GABAergic brain structures. Commun. Biol. *3*, 338. https://doi.org/10.1038/s42003-020-1028-8.

57. Bokulić, E., Medenica, T., Knezović, V., Štajduhar, A., Almahariq, F., Baković, M., Judaš, M., and Sedmak, G. (2021). The Stereological Analysis and Spatial Distribution of Neurons in the Human Subthalamic Nucleus. Front. Neuroanat. *15*, 749390. https://doi.org/10.3389/fnana.2021.749390.

58. Prasad, A.A., and Wallén-Mackenzie, Å. (2024). Architecture of the subthalamic nucleus. Commun. Biol. *7*, 78. https://doi.org/10.1038/s42003-023-05691-4.

59. Xu, W., Wang, J., Li, X.-N., Liang, J., Song, L., Wu, Y., Liu, Z., Sun, B., and Li, W.-G. (2023). Neuronal and synaptic adaptations underlying the benefits of deep brain stimulation for Parkinson's disease. Transl. Neurodegener. *12*, 55. https://doi.org/10.1186/s40035-023-00390-w.

60. Richter, E.O., Hoque, T., Halliday, W., Lozano, A.M., and Saint-Cyr, J.A. (2004). Determining the position and size of the subthalamic nucleus based on magnetic resonance imaging results in patients with advanced Parkinson disease. J. Neurosurg. *100*, 541–546. https://doi.org/10.3171/jns.2004.100.3.0541.

61. Haber, S.N. (2003). The primate basal ganglia: parallel and integrative networks. J. Chem. Neuroanat. *26*, 317–330. https://doi.org/10.1016/j.jchemneu.2003.10.003.

62. Parent, A., and Hazrati, L.N. (1995). Functional anatomy of the basal ganglia. II. The place of subthalamic nucleus and external pallidum in basal ganglia circuitry. Brain Res., Brain Res. Rev. *20*, 128–154. https://doi.org/10.1016/0165-0173(94)00008-d.

63. Parent, A., and De Bellefeuille, L. (1982). Organization of efferent projections from the internal segment of globus pallidus in primate as revealed by fluorescence retrograde labeling method. Brain Res. *245*, 201–213. https://doi.org/10.1016/0006-8993(82)90802-2.

64. Parent, M., Lévesque, M., and Parent, A. (2001). Two types of projection neurons in the internal pallidum of primates: single-axon tracing and three-dimensional reconstruction. J. Comp. Neurol. *439*, 162–175. https://doi.org/10.1002/cne.1340.

65. Miyamoto, Y., and Fukuda, T. (2022). New Subregions of the Mouse Entopeduncular Nucleus Defined by the Complementary Immunoreactivities for Substance P and Cannabinoid Type-1 Receptor Combined with Distributions of Different Neuronal Types. eNeuro *9*. ENEURO. 0208-22.2022. https://doi.org/10.1523/ENEURO.0208-22.2022.

66. Wallace, M.L., Saunders, A., Huang, K.W., Philson, A.C., Goldman, M., Macosko, E.Z., McCarroll, S.A., and Sabatini, B.L. (2017). Genetically Distinct Parallel Pathways in the Entopeduncular Nucleus for Limbic and Sensorimotor Output of the Basal Ganglia. Neuron *94*, 138–152.e5. https://doi.org/10.1016/j.neuron.2017.03.017.

67. Abdi, A., Mallet, N., Mohamed, F.Y., Sharott, A., Dodson, P.D., Nakamura, K.C., Suri, S., Avery, S.V., Larvin, J.T., Garas, F.N., et al. (2015). Prototypic and Arkypallidal Neurons in the Dopamine-Intact External Globus Pallidus. J. Neurosci. *35*, 6667–6688. https://doi.org/10.1523/JNEUROSCI.4662-14.2015.

68. Courtney, C.D., Pamukcu, A., and Chan, C.S. (2023). Cell and circuit complexity of the external globus pallidus. Nat. Neurosci. *26*, 1147–1159. https://doi.org/10.1038/s41593-023-01368-7.

69. Vieth, A., Kroes, T., Thijssen, J., van Lew, B. van, Eggermont, J., Basu, S., Eisemann, E., Vilanova, A., Höllt, T., and Lelieveldt, B. (2023). ManiVault: A Flexible and Extensible Visual Analytics Framework for High-Dimensional Data. IEEE Trans. Vis. Comput. Graph. *30*, 175–185. https://doi.org/10.1109/TVCG.2023.3326582.

70. Holt, D.J., Graybiel, A.M., and Saper, C.B. (1997). Neurochemical architecture of the human striatum. J. Comp. Neurol. *384*, 1–25. https://doi.org/10.1002/(SICI)1096-9861(19970721)384:1<1::AID-CNE1>3.0.CO;2-5.

71. Parent, A., Bouchard, C., and Smith, Y. (1984). The striatopallidal and striatonigral projections: two distinct fiber systems in primate. Brain Res. *303*, 385–390. https://doi.org/10.1016/0006-8993(84)91224-1.

72. Kraft, A.W., Lee, M., Rayan, N., Gao, H., Milidantri, J., Vanderburg, C., Balderrama, K., Nadaf, N., Kumar, V., Flowers, K., et al. (2026). Mesoscale molecular architecture of the human striatum across cell types and lifespan. Cell *189*, 7350–7368.e13. https://doi.org/10.1016/j.cell.2026.10.029.

73. Corbit, L.H., Muir, J.L., and Balleine, B.W. (2001). The role of the nucleus accumbens in instrumental conditioning: Evidence of a functional dissociation between accumbens core and shell. J. Neurosci. *21*, 3251–3260. https://doi.org/10.1523/JNEUROSCI.21-09-03251.2001.

74. Corbit, L.H., and Balleine, B.W. (2011). The general and outcome-specific forms of Pavlovian-instrumental transfer are differentially mediated by the nucleus accumbens core and shell. J. Neurosci. *31*, 11786–11794. https://doi.org/10.1523/JNEUROSCI.2711-11.2011.

75. Floresco, S.B. (2015). The Nucleus Accumbens: An Interface Between Cognition, Emotion, and Action. Annu. Rev. Psychol. *66*, 25–52. https://doi.org/10.1146/annurev-psych-010213-115159.

76. Haber, S.N., and Knutson, B. (2010). The reward circuit: linking primate anatomy and human imaging. Neuropsychopharmacology *35*, 4–26. https://doi.org/10.1038/npp.2009.129.

77. Jongen-Rêlo, A.L., Voorn, P., and Groenewegen, H.J. (1994). Immunohistochemical Characterization of the Shell and Core Territories of the Nucleus Accumbens in the Rat. Eur. J. Neurosci. *6*, 1255–1264. https://doi.org/10.1111/j.1460-9568.1994.tb00315.x.

78. Zahm, D.S., and Brog, J.S. (1992). On the significance of subterritories in the "accumbens" part of the rat ventral striatum. Neuroscience *50*, 751–767. https://doi.org/10.1016/0306-4522(92)90202-d.

79. Lazaridis, I., Crittenden, J.R., Ahn, G., Hirokane, K., Wickersham, I.R., Yoshida, T., Mahar, A., Skara, V., Loftus, J.H., Parvataneni, K., et al. (2024). Striosomes control dopamine via dual pathways paralleling canonical basal ganglia circuits. Curr. Biol. *34*, 5263–5283.e8. https://doi.org/10.1016/j.cub.2024.09.070.

80. Jung, W.H., Jang, J.H., Park, J.W., Kim, E., Goo, E.-H., Im, O.-S., and Kwon, J.S. (2014). Unravelling the Intrinsic Functional Organization of the Human Striatum: A Parcellation and Connectivity Study Based on Resting-State fMRI. PLoS One *9*, e106768. https://doi.org/10.1371/journal.pone.0106768.

81. Kosakowski, H.L., Saadon-Grosman, N., Du, J., Eldaief, M.C., and Buckner, R.L. (2024). Human striatal association megaclusters. J. Neurophysiol. *131*, 1083–1100. https://doi.org/10.1152/jn.00387.2023.

82. Pauli, W.M., O'Reilly, R.C., Yarkoni, T., and Wager, T.D. (2016). Regional specialization within the human striatum for diverse psychological functions. Proc. Natl. Acad. Sci. USA *113*, 1907–1912. https://doi.org/10.1073/pnas.1507610113.

83. Alkemade, A., and Forstmann, B.U. (2014). Do we need to revise the tripartite subdivision hypothesis of the human subthalamic nucleus (STN)? NeuroImage *95*, 326–329. https://doi.org/10.1016/j.neuroimage.2014.03.010.

84. Keuken, M.C., Uylings, H.B.M., Geyer, S., Schäfer, A., Turner, R., and Forstmann, B.U. (2012). Are there three subdivisions in the primate subthalamic nucleus? Front. Neuroanat. *6*, 14. https://doi.org/10.3389/fnana.2012.00014.

85. Marquand, A.F., Haak, K.V., and Beckmann, C.F. (2017). Functional corticostriatal connection topographies predict goal-directed behaviour in humans. Nat. Hum. Behav. *1*, 0146. https://doi.org/10.1038/s41562-017-0146.

86. Accolla, E.A., Herrojo Ruiz, M., Horn, A., Schneider, G.-H., Schmitz-Hübsch, T., Draganski, B., and Kühn, A.A. (2016). Brain networks modulated by subthalamic nucleus deep brain stimulation. Brain *139*, 2503–2515. https://doi.org/10.1093/brain/aww182.

87. Hamani, C., Florence, G., Heinsen, H., Plantinga, B.R., Temel, Y., Uludag, K., Alho, E., Teixeira, M.J., Amaro, E., and Fonoff, E.T. (2017). Subthalamic Nucleus Deep Brain Stimulation: Basic Concepts and Novel Perspectives. eNeuro *4*. ENEURO.0140-17.2017. https://doi.org/10.1523/ENEURO.0140-17.2017.

88. Alheid, G.F., Beltramino, C., Braun, A., Miselis, R.R., François, C., and De Olmos, J. (1994). Transition Areas of the Striatopallidal System with the Extended Amygdala in the Rat and Primate: Observations from Histochemistry and Experiments with Mono- and Transsynaptic Tracer. In The Basal Ganglia IV Advances in Behavioral Biology, G. Percheron, J.S. McKenzie, and J. Féger, eds. (Springer), pp. 95–107. https://doi.org/10.1007/978-1-4613-0485-2_9.

89. Fudge, J.L., and Tucker, T. (2009). Amygdala projections to central amygdaloid nucleus subdivisions and transition zones in the primate. Neuroscience *159*, 819–841. https://doi.org/10.1016/j.neuroscience.2009.01.013.

90. Li, H., Eid, M., Pullmann, D., Chao, Y.S., Thomas, A.A., and Jhou, T.C. (2021). Entopeduncular Nucleus Projections to the Lateral Habenula Contribute to Cocaine Avoidance. J. Neurosci. *41*, 298–306. https://doi.org/10.1523/JNEUROSCI.0708-20.2020.

91. Wallace, M.L., Huang, K.W., Hochbaum, D., Hyun, M., Radeljic, G., and Sabatini, B.L. (2020). Anatomical and single-cell transcriptional profiling of the murine habenular complex. eLife *9*, e51271. https://doi.org/10.7554/eLife.51271.

92. Hong, S., and Hikosaka, O. (2008). The globus pallidus sends reward-related signals to the lateral habenula. Neuron *60*, 720–729. https://doi.org/10.1016/j.neuron.2008.09.035.

93. Märtin, A., Calvigioni, D., Tzortzi, O., Fuzik, J., Wärnberg, E., and Meletis, K. (2019). A Spatiomolecular Map of the Striatum. Cell Rep. *29*, 4320–4333.e5. https://doi.org/10.1016/j.celrep.2019.11.096.

94. Smith, J.B., Klug, J.R., Ross, D.L., Howard, C.D., Hollon, N.G., Ko, V.I., Hoffman, H., Callaway, E.M., Gerfen, C.R., and Jin, X. (2016). Genetic-Based Dissection Unveils the Inputs and Outputs of Striatal Patch and Matrix Compartments. Neuron *91*, 1069–1084. https://doi.org/10.1016/j.neuron.2016.07.046.

95. Weglage, M., Wärnberg, E., Lazaridis, I., Calvigioni, D., Tzortzi, O., and Meletis, K. (2021). Complete representation of action space and value in all dorsal striatal pathways. Cell Rep. *36*, 109437. https://doi.org/10.1016/j.celrep.2021.109437.

96. Ishaque, N., Kharchenko, P., Lazic, D., Sun, J., Yang, J.Y.H., Emons, M., Heyl, F., Huber, W., Jones, D., Kuemmerle, L.B., et al. (2026). The Challenge of Cell Segmentation in Spatially Resolved Transcriptomics. Preprint at arXiv. https://doi.org/10.48550/arXiv.2606.09675.

97. Kunst, M., Ching, L., Quon, J., Mathieu, R., Hewitt, M.N., Seeman, S.C., Ayala, A., Gelfand, E.C., Long, B., Martin, N.X., et al. (2026). SCALPEL: A pipeline for processing large-scale spatial transcriptomics data. Preprint at bioRxiv. https://doi.org/10.64898/2026.01.09.698732.

98. Jones, D.C., Elz, A.E., Hadadianpour, A., Ryu, H., Glass, D.R., and Newell, E.W. (2025). Cell simulation as cell segmentation. Nat. Methods *22*, 1331–1342. https://doi.org/10.1038/s41592-025-02697-0.

99. Mitchel, J., Gao, T., Cole, E., Petukhov, V., and Kharchenko, P.V. (2026). Impact and correction of segmentation errors in spatial transcriptomics. Nature Genetics. https://doi.org/10.1038/s41588-025-02497-4.

100. Salas, S.M., Dammann, M., Rubens, R.K., Drummer, F., Halle, L., Becker, S., and Theis, F.J. (2025). Exploration of RNA outside segmented cells in spatial transcriptomics reveals extrasomatic RNA organization. Preprint at bioRxiv. https://doi.org/10.64898/2025.12.07.692889.

101. Miller, J. (2025). mfishtools: Building Gene Sets and Mapping mFISH Data, Version 0.0.2 (GitHub). https://github.com/AllenInstitute/mfishtools/tree/v0.0.2.

102. Missarova, A., Jain, J., Butler, A., Ghazanfar, S., Stuart, T., Brusko, M., Wasserfall, C., Nick, H., Brusko, T., Atkinson, M., et al. (2021). geneBasis: an iterative approach for unsupervised selection of targeted gene panels from scRNA-seq. Genome Biol. *22*, 333. https://doi.org/10.1186/s13059-021-02548-z.

103. Pachitariu, M., and Stringer, C. (2022). Cellpose 2.0: how to train your own model. Nat. Methods *19*, 1634–1641. https://doi.org/10.1038/s41592-022-01663-4.

104. Sofroniew, N., Lambert, T., Bokota, G., Nunez-Iglesias, J., Sobolewski, P., Sweet, A., Gaifas, L., Evans, K., Burt, A., Doncila Pop, D., et al. (2025). napari: a multi-dimensional image viewer for Python, [Version V0.6.6rc]2. Zenodo. https://doi.org/10.5281/zenodo.17311424.

105. Paxinos, G., Watson, C., Petrides, M., Rosa, M., and Tokuno, H. (2012). The Marmoset Brain in Stereotaxic Coordinates, First Edition (Academic Press).

106. Paxinos, G., Petrides, M., and Evrard, H. (2024). The Rhesus Monkey Brain in Stereotaxic Coordinates, Fourth Edition (Academic Press Elsevier).

107. Ding, S.L., Royall, J.J., Sunkin, S.M., Ng, L., Facer, B.A.C., Lesnar, P., Guillozet-Bongaarts, A., McMurray, B., Szafer, A., Dolbeare, T.A., et al. (2016). Comprehensive cellular-resolution atlas of the adult human brain. J. Comp. Neurol. *524*, 3127–3481. https://doi.org/10.1002/cne.24080.

108. Gillies, S., van der Wel, C., Van den Bossche, J., Taves, M.W., Arnott, J., Ward, B.C., et al. (2025). Shapely, [Version 2.1.2]. Zenodo. https://doi.org/10.5281/ZENODO.5597138.

109. Ahlmann-Eltze, C., and Huber, W. (2023). Comparison of transformations for single-cell RNA-seq data. Nat. Methods *20*, 665–672. https://doi.org/10.1038/s41592-023-01814-1.

110. Zhou, X., Dong, K., and Zhang, S. (2023). Integrating spatial transcriptomics data across different conditions, technologies and developmental stages. Nat Comput. Sci. *3*, 894–906. https://doi.org/10.1038/s43588-023-00528-w.

111. Morrison, M.L., and Rosenberg, N.A. (2023). Mathematical bounds on Shannon entropy given the abundance of the ith most abundant taxon. J. Math. Biol. *87*, 76. https://doi.org/10.1007/s00285-023-01997-3.

112. Kita, Y., Nishibe, H., Wang, Y., Hashikawa, T., Kikuchi, S.S., U, M., Yoshida, A.C., Yoshida, C., Kawase, T., Ishii, S., et al. (2021). Cellular-resolution gene expression profiling in the neonatal marmoset brain reveals dynamic species- and region-specific differences. Proc. Natl. Acad. Sci. USA *118*, e2020125118. https://doi.org/10.1073/pnas.2020125118.

113. Shimogori, T., Abe, A., Go, Y., Hashikawa, T., Kishi, N., Kikuchi, S.S., Kita, Y., Niimi, K., Nishibe, H., Okuno, M., et al. (2018). Digital gene atlas of neonate common marmoset brain. Neurosci. Res. *128*, 1–13. https://doi.org/10.1016/j.neures.2017.10.009.

114. Phipson, B., and Smyth, G.K. (2010). Permutation p-values should never be zero: calculating exact p-values when permutations are randomly drawn. Stat. Appl. Genet. Mol. Biol. *9*, 39. https://doi.org/10.2202/1544-6115.1585.

STAR★METHODS

KEY RESOURCES TABLE

REAGENT or RESOURCE	SOURCE	IDENTIFIER
Biological samples		
Rhesus macaque (*Macaca mulatta*) brain tissue	The Rockefeller University	QM23.50.001
Common marmoset (*Callithrix jacchus*) brain tissue	MIT	CJ23.56.004
Human (*Homo sapien*) brain tissue	University of Washington	H22.30.001
Critical commercial assays		
MERSCOPE v1.0 sample prep kit	Vizgen	PN 10400012
MERSCOPE 300 Gene Panel – macaque	Vizgen	BM1205
MERSCOPE 300 Gene Panel – human	Vizgen	BP1252
Xenium slides and sample prep reagents	10X	PN 1000460
Xenium decoding reagents	10X	PN 1000461
Xenium Cell Segmentation Kit	10X	PN 1000661
Xenium decoding consumables	10X	PN 1000487
Xenium v1 Standalone Custom 101 to 300 Gene Panel (16 rxn)	10X	PN 1000563, EU82Q4
Deposited data		
Marmoset spatial data	This paper	BIL: https://doi.org/10.35077/g.1211
Macaque spatial data	This paper	BIL: https://doi.org/10.35077/g.1211
Human spatial data	This paper	BIL: https://doi.org/10.35077/g.1211
Mouse spatial data	https://github.com/AllenInstitute/abc_atlas_access/blob/main/descriptions/MERFISH-C57BL6J-638850-imputed.md	RRID:SCR_024440
Software and algorithms		
Custom code for analysis and figure generation	https://github.com/AllenInstitute/BG_HMBA_Spatial	N/A
Xenium Analyzer Instrument	10X	PN 1000481, v3.0.2.0
Xenium Analyzer Onboard Analysis	10X	PN 1000481, v-xenium-3.0.0.15
Cellpose	https://www.cellpose.org/	RRID:SCR_021716
Spots in Space	https://github.com/AllenInstitute/spots-in-space/tree/main/sis	N/A
MapMyCells	https://github.com/AllenInstitute/cell_type_mapper	RRID:SCR_024672
mFISHtools	https://github.com/AllenInstitute/mfishtools	N/A
geneBasis	https://github.com/MarioniLab/geneBasisR	RRID:SCR_017257
Napari	https://github.com/napari/napari	RRID:SCR_022765
Shapely	https://github.com/shapely/shapely	RRID:SCR_027411
Cytosplore	viewer.cytosplore.org	RRID:SCR_018330
Scikit-learn	https://scikit-learn.org	RRID:SCR_002577
Scanpy	https://github.com/scverse/scanpy	RRID:SCR_018139
MetaNeighbor	https://github.com/gillislab/MetaNeighbor	RRID:SCR_016727
Scipy	https://scipy.org/	RRID:SCR_008058
OpenCV-python	https://github.com/opencv/opencv-python	RRID:SCR_015526

EXPERIMENTAL MODEL AND STUDY PARTICPANT DETAILS

Human

Donors 16–68 years of age with no known history of neuropsychiatric or neurological conditions ('control' cases) were considered for inclusion in this study. De-identified postmortem human brain tissue was collected after obtaining permission from the decedent's legal next-of-kin. Tissue collection was performed in accordance with the provisions of the United States Uniform Anatomical Gift Act of 2006 described in the California Health and Safety Code section 7150 (effective 1/1/2008) and other applicable state and federal laws and regulations. The Western Institutional Review Board (WIRB) reviewed the use of de-identified postmortem brain tissue for research purposes and determined that, in accordance with federal regulation 45 CFR 46 and associated guidance, the use of de-identified specimens from deceased individuals did not constitute human subjects research requiring IRB review. Routine serological screening for infectious disease (HIV, Hepatitis B, and Hepatitis C) was conducted using donor blood samples and donors negative for all three infectious diseases were considered for inclusion in the study. Tissue RNA quality was assessed using samples of total RNA derived from the frontal and occipital poles, which were processed on an Agilent 2100 Bioanalyzer using the RNA 6000 Nano kit to generate RNA Integrity Number (RIN) scores for each sample. The donor tissue featured in this study (HMBA ID: H22.30.001) originated from a 50-year-old Caucasian female who died of natural causes, with a postmortem interval of 8.1 hours. RIN values for this tissue upon intake were $\geq$8.0 for all regions assessed. At the point of block creation and data collection, RIN values specifically taken for the basal ganglia regions profiled were $\geq$8.0. The right hemisphere was profiled for spatial transcriptomics.

Macaque

The brain of one male Rhesus macaque monkey (HMBA ID: QM23.50.001) aged 10 years was collected for use in this study and the right hemisphere was profiled for spatial transcriptomics. All procedures for brain extraction were performed in The Rockefeller University's AAALAC accredited surgical suite under IACUC approved protocol# 24066-H and in compliance with all applicable federal and state animal welfare laws, regulations, and policy. In order to maximize the quality of the tissue to be subjected to gene-expression analysis, we attempted to minimize the time between the beginning of the transcardial perfusion and freezing. After initial sedation in the home cage using Ketamine ($\sim$3–10 mg/kg) plus Dexdomitor ($\sim$0.001–0.02 mg/kg) administered IM, the subject was intubated, and intravenous catheters were placed in the surgical suite. The subject was placed on a surgical table with heat support provided by a water recirculating blanket and a forced-air warming system, life support provided by a mechanical ventilator based on animal ETCO2 levels and maintained on intravenous lactated ringer's throughout the duration of anesthetized surgical procedures, and vital monitoring including respiratory rate, heart rate, blood pressure, end tidal CO2, Sp02 and core body temperature, and its head was placed in a stereotaxic frame. Once all vital parameters were stable, we established a plane of deep level of anesthesia using continuous infusions of intravenous fentanyl ($\sim$3–25 mcg/kg/hr) and dexdomitor ($\sim$1–3 mcg/kg/hr) along with gas isoflurane ($\sim$0.25%–2.5%). Level of anesthesia was confirmed using heart rate and toe pinch response as well as respiratory rate and palpebral response. Vitals and anesthesia levels were independently monitored by a veterinary technician and a veterinarian. Once this deep level of anesthesia was achieved, the skull was exposed and opened, and the dura mater removed. From this point on the brain was continuously flooded with a physiological saline solution to prevent it from drying. Upon confirmation of the depth of anesthesia by the veterinarian, transcardial perfusion was prepared by IV injection of pentobarbital sodium and phenytoin sodium at >150mg/kg to induce cardiac arrest. When this was confirmed by the veterinarian, an aortal catheter was introduced and transcardial perfusion with PBS 1X initiated, which lasted for ten minutes. Subsequently, the brain was removed in about two minutes and placed into a mold for slabbing (see below).

Marmoset

The brain of one five-year-old male marmoset (MIT ID 18–109, HMBA ID CJ23.56.004) was used in this study and the right hemisphere was profiled for spatial transcriptomics. All marmoset experiments were approved and conducted in compliance with the Massachusetts Institute of Technology CAC (IACUC) under protocol number 2303000479. The animal was initially sedated with Alfaxalone (12mg/kg, 10 mg/ml) and Midazolam (0.3 mg/kg, 5mg/ml) via intramuscular injection. They were further sedated with a secondary dose of Alfaxalone (4mg/kg, 10mg/ml) to ensure deep sedation followed by an intravenous injection of Euthasol (>120mg/kg, 390 mg/ml). When respiration and the pedal withdrawal reflex were eliminated, the marmosets were transcardially perfused with ice-cold carbogenated N-methyl-D-glucamine (NMDG) artificial cerebrospinal fluid (aCSF) (92 mM NMDG, 2.5 mM KCl, 1.25 mM NaH_2PO_4, 30 mM $NaHCO_3$, 20 mM HEPES, 25 mM glucose, 2 mM thiourea, 5 mM sodium L-ascorbate, 3 mM sodium pyruvate, 0.5 mM $CaCl_2 \cdot 2H_2O$, and 10 mM $MgSO_4 \cdot 7H_2O$; pH 7.3–7.4 adjusted with HCl). The brain was extracted from the skull and placed in ice-cold sucrose-HEPES. The brainstem and cerebellum were cut off and the brain was placed in a chilled brain mold and sliced with a razor blade into 5 mm slabs.

METHOD DETAILS

The experimental workflow, starting with the tissue harvested from each donor brain (Figure S1A) through to the final spatial transcriptomics dataset (Figure S1I), is schematized in Figure S1. Each point of the workflow is described in more detail below and briefly summarized here. Brain hemispheres were first cut into thick slabs and subsequently portioned into smaller blocks in the case of

macaque and human (Figure S1A). These tissues were sectioned into 10 μm sections (Figure S1B) for loading into the spatial transcriptomics platform of choice (Figure S1C). The resultant spatial transcripts were segmented into their cell of origin utilizing various signals of nuclear and cytoplasmic content (Figure S1D). From here, all data processing and analysis was performed on the cells and their gene expression. First, cells were subjected to quality control (QC) (Figure S1E, and see Figure S3), to remove low quality cells. Label transfer from the Basal Ganglia Cross-Species Consensus Taxonomy was performed with MapMyCells (RRID:SCR_024672) to assign basal ganglia cell type annotations (Figure S1F). In marmoset, the tissue was re-aligned to have the midline at vertical (Figure S1G). In macaque and human, the blocked data were stitched back together using block face tissue images acquired prior and during the steps outlined in B to create a mosaicked reconstruction of the full tissue (Figure S1H). The final dataset comprises the fully annotated basal ganglia cells sampled through the full rostral-caudal extent in each of the three species (Figures S1I).

Tissue processing

Slabbing

Fresh marmoset, macaque, and human hemispheres were slabbed in the coronal plane (Figure S1A) following the post-mortem brain processing procedure (https://dx.doi.org/10.17504/protocols.io.bf4ajqse). Marmoset tissue was slabbed at ∼5 mm thickness resulting in 6 slabs from rostral to caudal, 3 of which spanned basal ganglia (CX 42–44); macaque tissue was slabbed at ∼5–7 mm thickness resulting in 12 slabs, 5 of which spanned basal ganglia (CX 42–46); human tissue was slabbed at ∼4 mm thickness resulting in 60 slabs, 5 of which spanned basal ganglia (CX 13, 16–20). Slabs were flash frozen, vacuum sealed, and stored at -80°C until needed. Fresh and frozen slabs were photodocumented for downstream data alignment.

Blocking

Selected human and macaque slabs were equilibrated to -20°C for 1 hour prior to blocking (Figure S1A). Areas of interest within the slab were identified, outlined, and divided into blocks with a surface area smaller than that of the imaging area designated by the MERSCOPE platform. Blocking was performed while maintaining slabs and blocks at -20 C for the duration of the procedure. Each block and its relation to other blocks were photodocumented to ensure proper transformation of resulting data relative to other blocks and the slab as a whole.

Sectioning

Frozen tissue blocks were affixed to a sectioning chuck using Optimum Cutting Temperature medium (VWR 25608–930) and sectioned on a Leica cryostat at -17C at 10 μm onto Vizgen MERSCOPE coverslips (macaque and human) or 10X Xenium slides (marmoset). Marmoset hemispheres were kept intact for sectioning as they fit within the imaging window of 10X Xenium slides (Figure S1B). Sections from selected slabs were collected at 1 mm spacing intervals for macaque and human and at 200 μm intervals for marmoset (Figures 1A–1C). Final section intervals for marmoset vary from 200–600 μm due to instrument or per-section QC failures (also described in Dan et al.[33]). The sampling distance between slabs is variable and undefined due to a small amount of tissue loss at the beginning and end of the slab. Photos of the block face were taken prior to section collection for downstream data registration. Back-up sections for each primary one were collected and stored according to the platform specifications.

Gene panel design

Gene panels of up to 300 genes were designed for each species (300 each in marmoset and macaque, 299 in human) and spatial platform specifically with an effort to select overlapping genes when possible; 71 genes are shared across the three species gene panels (Table S2). The macaque and human MERSCOPE panels were designed in similar ways using a combination of tools. First, marker genes for the basal ganglia were manually curated with an effort toward selection of conserved genes across species. These were used as a starter list for two gene selection tools, mFISHtools[101] and geneBasis.[102] mFISHtools selects marker genes in a label-aware fashion with a supplied taxonomy, in this case an early version of the consensus taxonomy. In contrast, geneBasis selects genes label-free and instead tries to maximize the distance between a low-dimension manifold of reference RNA-seq data with all available genes and the same representation with the reduced gene selection. In this way, geneBasis can suggest genes that capture expression variance that is not captured in cell types, providing a complimentary approach to mFISHtools. The marmoset Xenium gene panel was similarly constructed as a combination of computationally and manually selected genes. The initial manual genes were selected from published marker genes, genes shared between human and macaque panels, and genes showing differential expression between caudate and putamen structures in the RIKEN ISH atlas (“Differential Search” tab at https://gene-atlas.brainminds.jp/gene-structural/). These genes served as starting genes for further computational search with geneBasis and mFISHtools using data from a previous study.[20]

After candidate gene panels for each species were designed, they were reviewed by 10X or Vizgen for compatibility with the relevant platform. Certain genes (e.g., *PVALB*) were replaced because they failed to meet technical requirements for probes such as transcript length, number of target sites, and expression level. In the case of the marmoset panel, iterations with the 10X probe design tool (https://www.10xgenomics.com/support/software/xenium-panel-designer/) also optimized the panel for utilization across cell types.

Spatial transcriptomics data acquisition

MERSCOPE

Sections were allowed to adhere to Vizgen MERSCOPE coverslips (Figure S1C) at room temperature for 10 minutes prior to a 1 minute wash in nuclease-free phosphate buffered saline (PBS) and fixation for 15 minutes in 4% paraformaldehyde in PBS. Fixation was

followed by 3x5 minute washes in PBS prior to a 1 minute wash in 70% ethanol. Fixed sections were then stored in 70% ethanol at 4C prior to use and for up to one month. Human sections were photobleached using a 240W LED array for 72 hours at 4°C (with temperature monitoring to keep samples below 17°C) prior to hybridization then washed in 5 mL Sample Prep Wash Buffer (VIZGEN 20300001) in a 5 cm petri dish. Sections were then incubated in 5 mL Formamide Wash Buffer (VIZGEN 20300002) at 37°C for 30 min. Sections were hybridized by placing 50 μL of VIZGEN-supplied Gene Panel Mix onto the section, covering with parafilm, and incubating at 37°C for 36-48 hours in a humidified hybridization oven. Following hybridization, sections were washed twice in 5 mL Formamide Wash Buffer for 30 minutes at 47°C. Sections were then embedded in acrylamide by polymerizing VIZGEN Embedding Premix (VIZGEN 20300004) according to the manufacturer's instructions. Sections were embedded by inverting sections onto 110 μL of Embedding Premix and 10% Ammonium Persulfate (Sigma A3678) and TEMED (BioRad 161-0800)[30] solution applied to a Gel Slick (Lonza 50640) treated 2x3 inch glass slide. The coverslips were pressed gently onto the acrylamide solution and allowed to polymerize for 1.5 hours. Following embedding, sections were cleared for 24–48 hours with a mixture of VIZGEN Clearing Solution (VIZGEN 20300003) and Proteinase K (New England Biolabs P8107S) according to the manufacturer's instructions. Following clearing, sections were washed 2x5 minutes in Sample Prep Wash Buffer (PN 20300001). VIZGEN DAPI and PolyT Stain (PN 20300021) was applied to each section for 15 minutes followed by a 10 minutes wash in Formamide Wash Buffer. Formamide Wash Buffer was removed and replaced with Sample Prep Wash Buffer during MERSCOPE set up. 100 μL of RNAse Inhibitor (New England BioLabs M0314L) was added to 250 μL of Imaging Buffer Activator (PN 203000015) and this mixture was added via the cartridge activation port to a pre-thawed and mixed MERSCOPE Imaging cartridge (VIZGEN PN1040004). 15 mL mineral oil (Millipore-Sigma m5904-6X500ML) was added to the activation port and the MERSCOPE fluidics system was primed according to VIZGEN instructions. The flow chamber was assembled with the hybridized and cleared section coverslip according to VIZGEN specifications and the imaging session was initiated after collection of a 10X mosaic DAPI image and selection of the imaging area. Specimens were imaged and automatically decoded into transcript location data.

Xenium

Fresh frozen tissue sections were mounted onto Xenium slides (10X Genomics, Figure S1C) and stored at −80 °C until use. Slides were equilibrated at 37 °C for 1 min using a pre-heated thermal cycler (Bio-Rad 1851197) equipped with a Xenium Thermocycler Adaptor. Fixation was performed in 1× PBS containing 2.5 mL paraformaldehyde (Electron Microscopy Sciences 15710) for 30 min at room temperature. Slides were permeabilized with 1% SDS (Millipore Sigma 71736) and incubated in pre-chilled 70% methanol for 60 min on wet ice.

Following permeabilization, slides were washed and transferred into Xenium cassettes. Probe hybridization was performed using a mix of Xenium Probe Hybridization Buffer, Probe Dilution Buffer, and either pre-designed or custom gene expression probes (10X Genomics). Probes were preheated at 95°C for 2 min and cooled on ice prior to mixing. Each slide received 500 μL of hybridization mix and was incubated overnight (16–24 h) at 50°C. Following hybridization, slides underwent washes using Xenium Post Hybridization Wash Buffer at 37°C. Ligation was performed by adding 500 μL of freshly prepared ligation mix containing Xenium Ligation Buffer, Enzyme A, and Enzyme B, followed by a 2 h incubation at 37°C. Amplification was conducted using a master mix of Xenium Amplification Mix and Enzyme, incubated for 2 h at 30°C. Autofluorescence quenching was achieved by sequential washes in TE buffer, 1x PBS, and ethanol solutions, followed by incubation with Xenium Autofluorescence Solution for 10 min in the dark. Nuclei staining was performed using Xenium Nuclei Staining Buffer, followed by four washes in PBS-T. Slides were stored in PBS-T at 4 °C or immediately processed for imaging.

Prepared slides were loaded into the Xenium Analyzer (10X Genomics 1000481) along with decoding reagent modules, buffer bottles, and consumables. Imaging buffers were freshly prepared, including Xenium Probe Removal Buffer and Sample Wash Buffers A and B. Reagents were loaded into designated positions on the instrument, and system checks were performed prior to initiating the run. Following the run, slides were scanned for DAPI and autofluorescence signals, and imaging regions were designated using the instrument's touchscreen interface. Imaging runs were initiated and completed over 1–3 days. Upon completion, fluidics cleanup was performed, and slides were stored in PBS-T at 4 °C. Imaging data were exported and reviewed for quality control.

Spatial data post-processing

Post-processing of the MERSCOPE and Xenium data was conducted utilizing custom tools with a focus on consistency and reproducibility across the three datasets (Figures S1D and S1E). While the MERSCOPE platform offers cell segmentation tools, we chose to re-segment macaque and human data with our custom segmentation pipeline[97] that shows improved data quality. The software is available on Github (https://github.com/AllenInstitute/spots-in-space/tree/main/sis). In brief, re-segmentation of the macaque and human MERSCOPE data was performed using a custom 3D Cellpose2.0[103] model that was trained on mouse, macaque, and human MERSCOPE data using the human-in-the-loop approach. The model utilized two channels, the DAPI image acquired during MERSCOPE acquisition and an image created from the total mRNA signal of the MERSCOPE data to approximate a cytosol stain (Figure S1D). Cell segmentation of marmoset data was performed on the Xenium instrument using the segmentation kit.

We used several quality control (QC) metrics to identify and remove low-quality cells, using the overall distributions of QC metrics within each dataset to select thresholds for filtering. In all three datasets, we filtered cells below a cutoff for total number of transcripts per cell (marmoset: 20, macaque: 20, human: 10) (Figure S4A). In macaque and human, we also applied a filter on the number of unique genes detected in each cell (macaque: 6, human: 4). Although we did not filter directly on the number of unique genes in marmoset, after filtering on total transcript counts, we observe no cells with fewer than 7 unique genes (Figure S4A). Cells in the

human dataset have on average fewer counts and unique genes per cell, resulting in lower QC thresholds and a smaller proportion of high-quality cells in human (76%) compared to marmoset (96%) and macaque (97%). Human samples require extensive light treatment to reduce autofluorescence prior to MERSCOPE imaging which may result in lower overall detection.

Additionally, the MERSCOPE gene panels include "blank" codewords that are not assigned to any real gene probe in the panel. These assess decoding error and can be utilized as a floor to the robustness of gene decoding. An upper limit of 2% of transcripts in a cell being assigned to a "blank" codeword was also applied to the macaque and human data (Figure S4B). All cells are included in the data release, but cells that do not meet the above QC thresholds are excluded from further analysis using the 'qc_pass' flag. Low-quality cells were also excluded from ABC atlas visualization.

Section and block alignment

The blocking procedure utilized for macaque and human tissue necessitated registration and stitching of sections, along with the spatial transcriptomics data, back to the original slab tissue coordinates (Figure S1H). Spatial transcriptomic sections were first registered to their corresponding block-face images using affine transformations. Visual inspection confirmed that tissue deformations in the imaged sections were minimal relative to the block-face images acquired immediately prior to sectioning. Block-face images were subsequently registered to slab tissue images to anchor the sections in slab space. The resulting stitched spatial transcriptomics image thus represents the same sectioning plane across independent blocks and was treated as a continuous coronal plane in downstream analysis which we refer to as a "slab-plane" (Figure S1I). Prior to registration, image scales were normalized and orientations were standardized to neurological convention (right hemisphere displayed on the right). Tissue cut surfaces were segmented and cropped to isolate the relevant block-face and slab-face regions, removing background and extraneous tissue outside the section plane. Anatomical landmarks were manually identified to perform affine registration between the block-face section most closely corresponding to each slab image. Finally, block-face images across consecutive sections within each block were aligned by matching cut edges and ensuring continuity of anatomical features between adjacent mosaicked blocks.

Manual anatomical annotations

To place the spatial transcriptomics data into the context of anatomical regions, manual outlines for the five major regions of the basal ganglia (STR, GPe, GPi, STH, SN) were drawn onto every section for all three species (Figure S19). Though these do not necessarily align exactly with the corresponding regions in the Harmonized Ontology of Mammalian Brain Anatomy (HOMBA),[23] the same acronyms are used for consistency. Additionally, consistent with HOMBA ontology, we refer to the longitudinal axis (front to back) of these structures as rostral (R) to caudal (C). Manual anatomical annotations were drawn using the polygon tool in napari (RRID:SCR_022765).[104] For the marmoset data, the Xenium cell segmentation kit stains were used to identify boundaries between white and grey matter. Further anatomical delineations were drawn using a combination of stains and marker gene expression (Figure S19A, Table S8). The marmoset Paxinos atlas was used as a reference[105] (Figures S20A–S20C). For the macaque and human MERSCOPE data, which did not include additional stains, annotations were drawn using a combination of marker gene expression (Figures S19B and S19C), cell density, and spatial domains (see "Spatial domain detection" below). The macaque Paxinos atlas[106] (Figures S20D–S20G) and the Allen Human Brain Atlas[107] (Figures S20H–S20K) were used as references. Finally, shapely's (RRID:SCR_027411)[108] "contains" function was used to label the cells that fell inside each of the manual annotation polygons drawn in napari. As the manually drawn polygons sometimes overlapped, cells were allowed to belong to multiple anatomical annotations.

Anatomical orientation across species to reference atlases

To inform our anatomical orientations and match sections across species, we found matching plates in reference atlases for each of our spatial sections, a subset of which are shown in Figure S20. This process involved scrolling through the coronal planes and using cues as described above (anatomical landmarks, spatial domains, etc.). Slab and blockface images registered to our spatial transcriptomics data provided additional anatomical context. Once structures were identified and, in some cases, manually annotated, we used the overall shape and relative locations of the structures to identify the best matching plate in the reference atlas. The angle of slicing was often not perfectly perpendicular to the coronal plane and thus in some cases, multiple plates were identified. The caudate tail represents a tricky example (Figures S21A–S21C) particularly in human. During extraction of human brain from the skull, the tissue is elongated, and structures toward the ventral end are stretched out of place. Using landmarks such as the optical tract (ot), we were able to reconstruct the proper orientation of this structure (Figures S21D and S21E).

QUANTIFICATION AND STATISTICAL ANALYSIS

Normalization

In our spatial transcriptomics datasets, we observe variation in overall detection between sections (Figure S22A; see also Figure S3). This can result in apparent discontinuities in gene expression across sections, which is particularly evident in macaque and human where multiple sections are registered together to create a coronal plane (Figure S1H). To standardize gene expression across sections for downstream processing, we applied a batch correction normalization. For each dataset, we calculate the mean total counts for all Astrocytes 1) within each section (per-section mean), and 2) for the entire dataset (dataset mean). Although there are varied populations of Astrocyte subtypes that have varied average transcript counts (Figure S22E), the correlation between Astrocyte

subtype fraction and Astrocyte total counts was low (Figure S22F). For each section, we then divide the dataset mean by the per-section mean to produce a correction factor, which we then multiply with the raw counts matrix (per-section correction factors: Table S11). This results in more consistent spatial gene expression across section boundaries (Figure S22D). Following batch normalization, we apply log transformation, which helps to stabilize variance[109] and enables comparison with single-cell RNA-seq data. It is common practice in measurements of transcript counts derived from techniques like RNA-seq and spatial transcriptomics to normalize and transform the raw counts data to account for variable detection across samples.[109]

Spatial domain detection

For the macaque and human datasets, domain detection was performed on binned transcript locations using STAligner.[110] Binned transcripts were used rather than segmented cells to account for GPU memory limitations. For macaque, transcripts were assigned to 50 micron square bins and bins with fewer than 60 unique genes were filtered out. For human, transcripts were assigned to 50 μm square bins and bins with fewer than 30 unique genes were filtered out. STAligner embedding was run on all sections from a species, with each section being considered a separate subgraph for training and transferred to cell space. Following the embedding, clustering was performed on the aligned latent space. For macaque, the leiden algorithm was used with resolution 0.8 and 15 nearest neighbors. For human, the mclust algorithm was used to identify 10 clusters.

Cell type mapping

Cells from each species were mapped to their respective snRNA-seq reference datasets using MapMyCells' (RRID:SCR_024672) (Figure S1F) flat mapping algorithm with bootstrapping (100 iterations, bootstrap factor 0.95). For marmoset, a full subcortex snRNA-seq taxonomy published concurrently[33] with v3 Clusters was used as a reference. For macaque and human, the snRNA-seq preprint taxonomy with Adjacent Clusters was used as a reference. The majority of Groups are represented in the snRNA-seq reference for all species, though some immune types, such as B-Cells, are more difficult to sample in nonhuman primate species. Given the mapping approach, Groups that are absent in a species reflects a lack of sampling in the taxonomy. We show all Groups in Figure 1F for completeness and in many subsequent figures focus on shared Groups across species. Cluster Human-382 was removed from the human reference before mapping due to poor quality, and Cluster Human-23 was reassigned from *STRd* D1 Striosome SPN to STRd D1 Matrix SPN after mapping.

Self-mapping of the snRNA-seq reference data was performed using the only species-specific gene panels to assess the goodness of label transfer (Figure S2). From this confusion matrix (Figures S2A–S2C) F1 scores for each Group (Figures S2D–S2F, blue bars) were calculated. We also calculated F1 scores of self-mapping utilizing all snRNA-seq genes (Figures S2D–S2F, orange bars). The F1 scores from these two self-mapping approaches are highly correlated (Figures S2G and S2D–S2F, scatter plots) with a ratio near one for all three species, giving us confidence that cell type mapping with the spatial gene panels is nearing the limit of the snRNA-seq taxonomy. MapMyCells uses correlation of gene expression between the reference and query data, in this case spatial transcriptomics data, to assign cell type labels. Each cell is assigned a label for the cell type with the highest correlation over 100 iterations, where in each iteration, 95% of the genes in the gene panel are randomly selected. The F1 scores show that the combinatorial effect of our 300 gene panels is sufficient for accurate label transfer, but we further show that expression of key marker genes for particular cell types are well correlated. Expression dot plots (Figures S2D–S2F) of conserved marker genes for SPNs (drawn from Johansen et al. Figure 2E) show similar Group-specific expression in both datasets across species.

To detect cells with low-quality or ambiguous mapping, we used the MapMyCells bootstrapping results (parameters used: 100 iterations, bootstrap factor 0.95). During bootstrapping, the gene panel is resampled and mapping is performed multiple times. Each cell is assigned to the most frequent type, and the bootstrapping probability reflects how often this type was assigned; the probabilities of the remaining "runner-up" types are also recorded. To incorporate both the bootstrapping probability and number of runners-up into a single metric, we calculated the Shannon entropy at the Group level using the bootstrapping and runner-up probabilities for each cell (Figures S4D and S4E). Plotting bootstrapping probability versus entropy recapitulates a relationship that has been described in species abundance data: as the number of possible species (or cell type assignments) increases, the upper and lower bounds of Shannon entropy increase in a predictable pattern (Figure S4D).[111] A threshold of 0.7 was used, which approximates the upper bound of Shannon entropy for a cell with a bootstrapping probability of 0.5 with one runner-up. The majority of our data has an entropy below this threshold (marmoset: 97%; macaque: 98%; human: 95%) (Figure S4D). Groups with a higher proportion of cells above the threshold, such as ZI-HTH, are outside of basal ganglia regions and therefore expected to have low-confidence mapping (Figure S4E).

Data inclusion criteria

Data used for further analysis included only those cells that passed cell-segmentation QC ('qc_pass'), was within the boundaries of the manually annotated basal_ganglia_and_adjacent region, and mapped robustly (Group Shannon entropy < 0.7) to the Basal Ganglia Consensus Taxonomy. This results in the following cell counts for each species used in downstream analysisl; marmoset: 1,299,927 cells, macaque: 3,117,043 cells, human: 4,025,134 cells. Data was organized from most rostral to most caudal and is presented in figures as such (ex. Figures 1A–1C).

Compartment masks

Polygon masks for the three compartments in the striatum were generated from the cells belonging to their associated Groups: striosomes (STRd D1 Striosome SPN, STRd D2 Striosome SPN), ICjs (OT ICj Granule), and NUDAPs (STRv D1 NUDAP eSPN, STR D1D2 eSPN). 2D compartment polygon masks were constructed within each individual two-dimensional slab-plane. For each compartment, cells with the Group labels were initially filtered to remove extreme outliers using, first, a KNN with 5 nearest neighbors and then scipy's (RRID:SCR_008058) DBSCAN algorithm (minimum cluster size, all species: 10 cells). Remaining cells were binned (marmoset: 20 μm; macaque: 50 μm; human: 80 μm) and converted to a binary mask. After applying scipy's ndimage module's "binary_closing" and "binary_fill_holes" functions, the binary masks were converted first to contours using opencv-python (RRID:SCR_015526) and then to shapely polygons. Individual polygons were given unique identifiers. Using shapely's "contains" function, cells were assigned to the specific polygon they fell within.

Cell type enrichment in compartments

Enrichment was calculated per section and defined as the change in the number of cells observed inside the compartment when compared to a null distribution. To generate the null distribution, 10,000 iterations of label permutation were run. In each iteration, cell type labels for all cells inside the striatum manual annotation polygons were shuffled, and the number of cells observed within the compartment was counted. The mean and standard deviation of all iterations were combined and the overall mean and standard deviation calculated. The per-section enrichment was z-scored as:

$$((\text{counts_observed}) - \text{mean}(\text{counts_nulldist})) \ / \ \text{std}(\text{counts_nulldist})$$

Sections that did not meet minimum criteria for either cell counts for that Group or null distribution statistics were excluded (cells_in_Group_per_section $\leq$20; null_dist_mean $\leq$5; null_CV $\leq$0.5). For each section, empirical one-sided p-values (one for enrichment, one for depletion) were calculated directly from the null distribution of counts, and a Benjamini-Hochberg false detection rate (FDR) correction (alpha=0.01) was applied.

MetaNeighbor

The python implementation of MetaNeighbor (pMN; https://github.com/gillislab/pyMN) was run in unsupervised mode with the study label set to "modality" (snRNA-seq versus spatial data; study_col="modality", ct_col="Group", fast_version=True, symmetric_output=False). AUROC similarity scores for each 2x2 block (one Group, snRNA-seq vs spatial) were averaged and displayed as annotated text on the similarity matrix. MetaNeighbor documentation recommends that AUROC scores$\geq$0.9 be considered the same cell type.

Calculation of distance to nearest striosome compartment

In individual 2D slab-planes, distances from every cell to every striosome polygon boundary were computed via shapely's "distance" function. Each cell was assigned to the polygon with the nearest boundary and given a "nearest_poly_min_distance". Shapely's "contains" function was used to distinguish cells inside and outside the polygons, which were assigned "inside_distance" and "outside_distance", respectively. Outside distances were used for determining status of striosome-like cells that are found outside striosome masks.

Striosome versus Matrix SPN scores

Spatial transcriptomic data were subset and organized into two categories: Striosome SPN (including STRd D1 Striosome SPN and STRd D2 Striosome SPN Group cells) and Matrix SPN (STRd D1 Matrix SPN and STRd D2 Matrix SPN Group cells), the same labels from the MapMyCells label transfer described above. Expression was batch-corrected and natural logarthim transformed, as described above, on the full dataset prior to any model fitting or cross-validation. An L2-penalized logistic regression model was fit on all spatial data per species using sklearn's (RRID:SCR_019053) "linear_model.LogisticRegression" (parameters: C=10, solver='saga', max_iter=500) with a binary outcome (Striosome SPN versus Matrix SPN). Curated species-specific marker genes (all species: *KCNIP1*, *BACH2*; human: *LOXHD1*; macaque: *SPON1*, *TSHZ1*, *BRINP3*, *GALNTL6*; marmoset: *SPON1*, *GRIN3A*, *PHACTR2*) were weighted to ensure canonical markers were included in the model. Feature weighting and remaining marker gene set selection was determined globally during this all-slab-plane model training. Summed counts of the top 20 genes with positive coefficients (striosome factor) and top 20 with negative coefficients (matrix factor) from this global training were used as an additional interpretable striosome vs matrix score. Cells were assigned a final striosome decision score via sklearn's "StratifiedGroupKFold" and "cross_val_predict" grouped by slab-plane ("z_order") (parameters: n_splits=5, shuffle=True, groups="z_order", method="decision_function"). Thresholds to determine a "high striosome score" (describe more below) were set on the raw log-odds with positive values indicating more striosome-like identity.

Candidate striosome-like cell inclusion criteria

To identify candidate striosome-like cells that are located outside of striosome masks, we implemented two criteria. We considered only Striosome SPNs that were: (1) a sufficient two-dimensional distance from a striosome mask boundary within a two-dimensional

slab-plane (≥100 μm in marmoset, ≥200 μm in macaque, and ≥400 μm in human) to correct for small errors or fluctuations in the compartment mask definition, and (2) had a high striosome logistic regression decision score (> mean + 1 std of the log-odds distribution of all striosome-like cells; absolute scores of >5.5 in marmoset, 8.9 in macaque, and 5.6 in human). Across species, roughly half of cells labeled as Striosome SPNs by our original mapping (marmoset: 51.0%, macaque 47.0%, human: 54.7%) are located outside the striosome masks. 49–53% of those cells (marmoset: 49.2%; macaque 52.8%; human: 50.6%) are ruled out by Criteria 1 as having been missed by the initial masking procedure. A further 45%–48% of these cells (marmoset 48.1%, macaque 44.9%, human 47.4%) have some potential to be confused for Matrix SPNs based on their gene expression profile as defined by the strict Criteria 2. This leaves the remaining cells (marmoset 2.7%, macaque 2.2%, human 2.0%; representing 1.4% marmoset, 1.1% macaque, and 1.0% human, of all mapped Striosome SPNs cells, respectively; n = 1,142, 1,317 and 1,140 cells, respectively) as candidate cells with strong striosome-like gene expression (Criteria 2) that are plausibly far from a striosome mask in the same two-dimensional slab-plane (Criteria 1). Absolute counts of all Striosome SPN cells and candidate striosome-like cells outside of striosome masks, reported by species, slab-plane, and D1 vs D2 identity, can be found in Table S10. We note that Criteria 1 is unable to account for or entirely exclude the possibility of a nearby striosome in the third dimension.

Principal component analysis (PCA) and gradient analysis

Non-spatial PCA was run on SPN Group cells in each species independently using scanpy's (RRID:SCR_018139) PCA function. After filtering out genes with mean batch-corrected expression of 0.25, we ran PCA on the batch-corrected and natural logarithm transformed gene expression. We defined the gradient PC (PCg) as the PC with the highest gradient score (Figure S12B), which measures the distance between the centroid of cells with PC values less than the 20th percentile and the centroid of cells with PC values greater than the 80th percentile. This score is large for PCs with graded values over large spatial extent and small for PCs with spatially random or finely structured variation. The angle of the PCg was calculated as the 2D gradient of PCg on the cells in each section, which corresponded to the approximate internal capsule axis (Figure S12C). For visualization in the quiver plots in Figure 4C, the arrow is plotted at the angle from the mean of all PCg gradient angles. To reduce overlapping of the plotted arrows, the mean PCg angle was set to be vertical. We confirmed gradient expression of individual genes with inspection of their transcript density derived from the MERSCOPE or Xenium spatial transcriptomics data at two extreme positions (Figure S23) as well as comparing to reference *in situ* hybridization (ISH) atlases for marmoset (RIKEN Marmoset Gene Atlas)[112,113] and macaque (Blueprint NHP Atlas, https://www.blueprintnhpatlas.org/).

To assess the robustness of PCg, we performed two additional analyses. First, we performed a hold-out analysis (Figures S12E and S12F). One slab-plane was held out (held-out plane), and scaling and PCA was performed on all other slab-planes (the training set) using the same parameters as for the original PCA. The training set loadings were then applied to the held-out plane, and the resulting held-out PCs were matched to the original PCs using the orthogonal Procrustes function from the scipy package (scipy.linalg.orthogonal_procrustes). To assess the agreement of the held-out PCs to the original PCs, Tucker's congruence coefficient, Spearman correlation of gene loadings for all genes, and Pearson correlation of the per-cell PC scores on the held-out plane were calculated. Second, we performed a permutation (null) analysis to assess the likelihood that the spatial organization of PCg could have arisen by chance during the PCg selection procedure (Figure S12G). The data were subset to the slab-planes initially used to identify the gradient PC, and PC scores were shuffled with respect to the cell positions within each slab-plane over 1000 permutations. In each permutation, the gradient score was recalculated for the top 10 PCs – the same number of PCs considered during the original selection – and the highest gradient score across these 10 PCs was retained to create a null distribution. The observed PCg's gradient score was compared to the null distribution, and the permutation p-value was computed as in Phipson and Smyth 2016.[114]

Contour plots

Each section was divided into 2D rectangular bins at a resolution of 120 bins along each of the x and y axes. The sum of the per-cell gradient PCg values and the number (count) of cells were calculated for each bin. Both the sums and counts were smoothed using a 2D Gaussian filter, where the degree of smoothing (sigma) was specified in physical units (marmoset: 150 μm; macaque: 300 μm; human: 600 μm) and converted to bin units to ensure that despite differences in section size and bin size, the degree of smoothing was consistent across sections. The smoothed sum was then divided by the smoothed counts to obtain a smoothed local average of the PCg. Bins with centers farther than a threshold distance from the nearest cell (marmoset: 50 μm; macaque: 100 μm; human: 200 μm) were masked out to avoid extrapolating beyond tissue edges. To ensure contour levels were comparable across sections, the smoothed local average values for all sections within a species were aggregated and discretized into 12 equal width levels.

DEG dot plots

Differentially expressed gene (DEG) detection for STH, striosome, and STRv Cluster analysis was performed using scanpy's ''rank_genes_groups'' function (method=''wilcoxon'').

Mouse data

Mouse spatial transcriptomics data is part of the Allen whole mouse brain cell type atlas[13] and is available for download through the ABC Atlas (RRID:SCR_024440). Datasets MERFISH-C57BL6J-638850 with Imputed Genes + Reconstructed Coordinates and MERFISH-C57BL6J-638850 Reconstructed Coordinates were used in Figure S11A and for comparison with primate species in the GP (Figures S17B and S17D).

Cytosplore Gradient Surfer

Gradient Surfer is a plugin for the Cytosplore Viewer data visualization system,[69] available at https://viewer.cytosplore.org including spatial data from this paper. Starting with one dataset as reference, the user can interactively select cells from the data, e.g., cells of the dorsal striatum, in a linear strip along the internal capsule axis. Cell positions of selected cells are projected on the line, and Pearson correlation is calculated between the expression profiles of the shared gene set and the projected cell coordinates. This reveals genes whose expression consistently varies with or against the line coordinate, reflecting a gradient along the drawn line. Principal Component Analysis (PCA) is applied to the matrix of the selected cells by the top N gradient genes, resulting in a set of gradient PCs for the selected cells in the reference dataset. The PC with the strongest correlation with the linear position along the line is automatically selected.

The second dataset may be acquired with a different gene panel, but no line is selected, so a second PCA is performed on all cells in the second dataset, but only on the top N gradient genes as calculated in the reference dataset. The PC with the strongest correlation of the reference gradient PC is selected as the best match. Within each dataset, all genes are ordered by correlation with the strongest (or manually selected) gradient PC for that dataset. However, PC loadings can be visualized as color overlays on spatial scatterplots similar to the gene expression to verify which PC represents the probed gradient best. See Figure S18.

All abbreviations used in this manuscript are defined in Table S12.

ADDITIONAL RESOURCES

The data used in this paper are available for download alongside tutorials for programmatic access (https://brain-map.org/consortia/hmba/hmba-release-basal-ganglia). See Results section for further details.